

RAI 2-4:

Replace SAR Section 8.1.7 with the neutron absorber acceptance testing section currently in proposed TransNuclear (TN) Standardized NUHOMS CoC 1004, Amendment 10. Include the acceptance testing by reference to the SAR in the CoC.

The staff does not agree that this section as currently written adequately describes the necessary acceptance testing for neutron absorbers. Replacement with the section from CoC 1004, Amendment 10, makes the acceptance testing requirements for all the DSCs for both storage and transportation consistent.

This information is needed to satisfy 10 CFR 71.33 (a)(5)(ii) and 71.35.

RAI 2-4 Response:

Section A.8.1.7 of the SAR has been revised to include neutron absorber acceptance testing consistent with NRC approved acceptance testing in Amendment 10 of CoC 1004, for DSCs which will be fabricated in the future.

Section A.8.1.7.2 has also been revised to account for DSCs that have been already loaded or previously fabricated.

RAI 2-4 SAR Changes to Section A.8.1.7

A.8.1.7. Neutron Absorber Tests

CAUTION

Sections A.8.1.7.1 through A.8.1.7.3 below are incorporated by reference into the CoC 9302 Conditions (paragraph tbd) and shall not be deleted or altered in any way without a CoC revision approval from the NRC. The text of these sections is shown in bold type to distinguish it from other sections.

The neutron absorber used for criticality control in the DSC baskets may consist of any of the following types of material. Depending of the DSC model, these neutron absorber materials may be used alone or be paired with aluminum:

- (a) Borated Aluminum
- (b) Boron carbide / Aluminum metal matrix composite (MMC)
- (c) Boral[®]

These materials only serve as neutron absorber for criticality control and as heat conduction path. The MP197HB safety analyses do not rely upon their mechanical

strength. The radiation and temperature environment in the cask is not sufficiently severe to damage these metallic/ceramic materials. To assure performance of the neutron absorber's design function only the presence of B10 and the uniformity of its distribution need to be verified, with testing requirements specific to each material.

References to metal matrix composites throughout this chapter are not intended to refer to Boral[®], which is described later in this section.

A.8.1.7.1 Borated Aluminum

See the Caution in Section A.8.1.7 before deletion or modification to this section.

The material is produced by direct chill (DC) or permanent mold casting with boron precipitating as a uniform fine dispersion of discrete AlB₂ or TiB₂ particles in the matrix of aluminum or aluminum alloy. For extruded products, the TiB₂ form of the alloy shall be used. For rolled products, either the AlB₂, the TiB₂, or a hybrid may be used.

Boron is added to the aluminum in the quantity necessary to provide the specified minimum B10 areal density in the final product, with sufficient margin to minimize rejection, typically 10 % excess. The amount required to achieve the specified minimum B10 areal density will depend on whether boron with the natural isotopic distribution of the isotopes B10 and B11, or boron enriched in B10 is used. In no case shall the boron content in the aluminum or aluminum alloy exceed 5% by weight.

The criticality calculations take credit for 90% of the minimum specified B10 areal density of borated aluminum. The basis for this credit is the B10 areal density acceptance testing, which shall be as specified in Section A.8.1.7.4. The specified acceptance testing assures that at any location in the material, the minimum specified areal density of B10 will be found with 95% probability and 95% confidence.

Visual inspections shall follow the recommendations in Aluminum Standards and Data, Chapter 4 "Quality Control, Visual Inspection of Aluminum Mill Products and Castings"[1]. Local or cosmetic conditions such as scratches, nicks, die lines, inclusions, abrasion, isolated pores, or discoloration are acceptable. Widespread blisters, rough surface, or cracking shall be evaluated for acceptance in accordance with the Certificate Holder's QA procedures.

A.8.1.7.2 Boron Carbide / Aluminum Metal Matrix Composites (MMC)

See the Caution in Section A.8.1.7 before deletion or modification to this section.

The material is a composite of fine boron carbide particles in an aluminum or aluminum alloy matrix. The material shall be produced by either direct chill casting, permanent mold casting, powder metallurgy, or thermal spray techniques. It is a low-porosity product, with a metallurgically bonded matrix. The boron

carbide content shall not exceed 40% by volume. The boron carbide content for MMCs with an integral aluminum cladding shall not exceed 50% by volume.

Prior to use in the DSC, MMCs shall pass the qualification testing specified in Section A.8.1.7.5, and shall subsequently be subject to the process controls specified in Section A.8.1.7.6.

The criticality calculations take credit for 90% of the minimum specified B10 areal density of MMCs. The basis for this credit is the B10 areal density acceptance testing, which is specified in Section A.8.1.7.4. The specified acceptance testing assures that at any location in the final product, the minimum specified areal density of B10 will be found with 95% probability and 95% confidence.

Visual inspections shall follow the recommendations in Aluminum Standards and Data, Chapter 4 “Quality Control, Visual Inspection of Aluminum Mill Products and Castings” [1]. Local or cosmetic conditions such as scratches, nicks, die lines, inclusions, abrasion, isolated pores, or discoloration are acceptable. Widespread blisters, rough surfaces, or cracking shall be evaluated for acceptance in accordance with the Certificate Holder’s QA procedures.

A.8.1.7.3 Boral[®]

See the Caution in Section A.8.1.7 before deletion or modification to this section.

This material consists of a core of aluminum and boron carbide powders between two outer layers of aluminum, mechanically bonded by hot-rolling an “ingot” consisting of an aluminum box filled with blended boron carbide and aluminum powders. The core, which is exposed at the edges of the sheet, is slightly porous. The average size of the boron carbide particles in the finished product is approximately 85 microns before rolling. The nominal boron carbide content shall be limited to 65% (+ 2% tolerance limit) of the core by weight.

The criticality calculations take credit for 75% of the minimum specified B10 areal density of Boral[®]. B10 areal density will be verified by chemical analysis and by certification of the B10 isotopic fraction for the boron carbide powder, or by neutron transmission testing. Areal density testing is performed on an approximately 1 cm² area of a coupon taken near one of the corners of the sheet produced from each ingot. If the measured areal density is below that specified, all the material produced from that ingot will be either rejected, or accepted only on the basis of alternate verification of B10 areal density for each of the final pieces produced from that ingot.

Visual inspections shall verify that the Boral[®] core is not exposed through the face of the sheet at any location.

A.8.1.7.4 Specification for Acceptance Testing of Neutron Absorbers by Neutron Transmission

CAUTION

Section A.8.1.7.4 is incorporated by reference into the CoC 9302 Conditions (paragraph tbd) and shall not be deleted or altered in any way without a CoC revision approval from the NRC. The text of this section is shown in bold type to distinguish it from other sections.

Neutron Transmission acceptance testing procedures shall be subject to approval by the Certificate Holder. Test coupons shall be removed from the rolled or extruded production material at locations that are systematically or probabilistically distributed throughout the lot. Test coupons shall not exhibit physical defects that would not be acceptable in the finished product, or that would preclude an accurate measurement of the coupon's physical thickness.

A lot is defined as all the pieces produced from a single ingot or heat or from a group of billets from the same heat. If this definition results in lot size too small to provide a meaningful statistical analysis of results, an alternate larger lot definition may be used, so long as it results in accumulating material that is uniform for sampling purposes.

The sampling rate for neutron transmission measurements shall be such that there is at least one neutron transmission measurement for each 2000 square inches of final product in each lot.

The B10 areal density is measured using a collimated thermal neutron beam of up to 1.2 centimeter diameter. A beam size greater than 1.2 centimeter diameter but no larger than 1.7 centimeter diameter may be used if computations are performed to demonstrate that the calculated $k_{\text{effective}}$ of the system is still below the calculated Upper Subcritical Limit (USL) of the system assuming defect areas the same area as the beam.

The neutron transmission through the test coupons is converted to B10 areal density by comparison with transmission through calibrated standards. These standards are composed of a homogeneous boron compound without other significant neutron absorbers. For example, boron carbide, zirconium diboride or titanium diboride sheets are acceptable standards. These standards are paired with aluminum shims sized to match the effect of neutron scattering by aluminum in the test coupons. Uniform but non-homogeneous materials such as metal matrix composites may be used for standards, provided that testing shows them to provide neutron attenuation equivalent to a homogeneous standard.

Alternatively, digital image analysis may be used to compare neutron radioscopic images of the test coupon to images of the standards. The area of image analysis

shall be up to 1.1 cm². The method shall demonstrate sufficient sensitivity to distinguish between areal density at the specified minimum, and 1% above and below the minimum.

The minimum areal density specified shall be verified for each lot at the 95% probability, 95% confidence level or better. The following illustrates one acceptable method.

The acceptance criterion for individual plates is determined from a statistical analysis of the test results for their lot. The minimum B10 areal densities determined by neutron transmission are converted to volume density, i.e., the minimum B10 areal density is divided by the thickness at the location of the neutron transmission measurement or the maximum thickness of the coupon. The lower tolerance limit of B10 volume density is then determined, defined as the mean value of B10 volume density for the sample, less K times the standard deviation, where K is the one-sided tolerance limit factor with 95% probability and 95% confidence [2]. If a goodness-of-fit test demonstrates that the sample comes from a normal population, the value of K for a normal distribution may be used. Otherwise, use a non-parametric (distribution-free) method of determining the one-sided tolerance limit.

Finally, the minimum specified value of B10 areal density is divided by the lower tolerance limit of B10 volume density to arrive at the minimum plate thickness which provides the specified B10 areal density.

Any plate which is thinner than this minimum or the minimum design thickness, whichever is greater, shall be treated as non-conforming, with the following exception. Local depressions are acceptable, so long as they total no more than 0.5% of the area on any given plate, and the thickness at their location is not less than 90% of the minimum design thickness.

Non-conforming material shall be evaluated for acceptance in accordance with the Certificate Holder's QA procedures.

A.8.1.7.5 Specification for Qualification Testing of Metal Matrix Composites

A.8.1.7.5.1 Applicability and Scope

Metal matrix composites (MMCs) shall consist of fine boron carbide particles in an aluminum or aluminum alloy matrix. The ingot shall be produced by either powder metallurgy (PM), thermal spray techniques, or by direct chill (DC) or permanent mold casting. In any case, the final MMC product shall have density greater than 98% of theoretical, a metallurgically bonded matrix, and boron carbide content no greater than 40% by volume. (For MMCs with an integral aluminum cladding, the maximum boron carbide content shall be no greater than 50% by volume and the density shall be greater than 97% of theoretical density.) Boron carbide particles for the products considered here typically have an average size in the range 10-40 microns, although the actual specification may be by mesh size, rather than by average particle size. No more than

10% of the particles shall be over 60 microns. The material shall have negligible interconnected porosity exposed at the surface or edges.

Prior to initial use in a spent fuel dry storage or transport system, such MMCs shall be subjected to qualification testing that will verify that the product satisfies the design function. Key process controls shall be identified per Section A.8.1.7.6 so that the production material is equivalent to or better than the qualification test material. Changes to key processes shall be subject to qualification before use of such material in a spent fuel dry storage or transport system.

ASTM test methods and practices are referenced below for guidance. Alternative methods may be used with the approval of the certificate holder.

A.8.1.7.5.2 Design Requirements

In order to perform its design functions the product must have at a minimum sufficient strength and ductility for manufacturing and for the normal and accident conditions of the storage/ transport system. This is demonstrated by the tests in Section A.8.1.7.5.4. It must have a uniform distribution of boron carbide. This is demonstrated by the tests in Section A.8.1.7.5.5.

A.8.1.7.5.3 Durability

There is no need to include accelerated radiation damage testing in the qualification. Such testing has already been performed on MMCs, and the results confirm what would be expected of materials that fall within the limits of applicability cited above. Metals and ceramics do not experience measurable changes in mechanical properties due to fast neutron fluences typical over the lifetime of spent fuel storage, about 10^{15} neutrons/cm².

The need for thermal damage and corrosion (hydrogen generation) testing shall be evaluated case-by-case based on comparison of the material composition and environmental conditions with previous thermal or corrosion testing of MMCs.

Thermal damage testing is not required for MMCs consisting only of boron carbide in an aluminum 1100 matrix, because there is no reaction between aluminum and boron carbide below 842°F, well above the basket temperature under normal conditions of storage or transport¹.

Corrosion testing is not required for full density MMCs consisting only of boron carbide in an aluminum 1100 matrix, because testing on one such material has already been performed by Transnuclear².

¹ Sung, C., "Microstructural Observation of Thermally Aged and Irradiated Aluminum/Boron Carbide (B₄C) Metal Matrix Composite by Transmission and Scanning Electron Microscope," 1998.

² Boralyn testing submitted to the NRC under docket 71-1027, 1998.

A.8.1.7.5.4 Required Qualification Tests and Examinations to Demonstrate Mechanical Integrity

At least three samples, one each from the two ends and middle of the test material production run shall be subject to:

- a) room temperature tensile testing (ASTM- B557³) demonstrating that the material has the following tensile properties:
- Minimum yield strength, 0.2% offset: 1.5 ksi
 - Minimum ultimate strength: 5 ksi
 - Minimum elongation in 2 inches: 0.5%
- (Alternatively show that the material fails in a ductile manner, e.g., by scanning electron microscopy of the fracture surface or by bend testing.)

and

- b) testing (ASTM-B311⁴) to verify more than 98% (or 97% for MMCs with integral aluminum cladding) of theoretical density. Testing or examination for exposed interconnected porosity shall be performed by a means to be approved by the Certificate Holder.

A.8.1.7.5.5 Required Tests and Examinations to Demonstrate B10 Uniformity

CAUTION

Section A.8.1.7.5.5 is incorporated by reference into the CoC 9302 Conditions (paragraph tbd) and shall not be deleted or altered in any way without a CoC revision approval from the NRC. The text of this section is shown in bold type to distinguish it from other sections.

Uniformity of the boron distribution shall be verified either by:

- a) **Neutron radioscopy or radiography (ASTM E94⁵, E142⁶, and E545⁷) of material from the ends and middle of the test material production run, verifying no more than 10% difference between the minimum and maximum B10 areal density, or**
- b) **Quantitative testing for the B10 areal density, B10 density, or the boron carbide weight fraction, on locations distributed over the test material**

³ ASTM B557 Standard Test Methods of Tension Testing Wrought and Cast Aluminum and Magnesium-Alloy Products.

⁴ ASTM B311, Test Method for Density Determination for Powder Metallurgy (P/M) Materials Containing Less than Two Percent Porosity

⁵ ASTM E94, Recommended Practice for Radiographic Testing

⁶ ASTM E142, Controlling Quality of Radiographic Testing

⁷ ASTM E545, Standard Method for Determining Image Quality in Thermal Neutron Radiographic Testing

production run, verifying that one standard deviation in the sample is less than 10% of the sample mean. Testing may be performed by a neutron transmission method similar to that specified in Section A.8.1.7.4, or by chemical analysis for boron carbide content in the composite.

A.8.1.7.5.6 Approval of Procedures

Qualification procedures shall be subject to approval by the Certificate Holder.

A.8.1.7.6 Specification for Process Controls for Metal Matrix Composites

A.8.1.7.6.1 Applicability and Scope

The applicability of this section is the same as that of Section A.8.1.7.5. It addresses the process controls to ensure that the material delivered for use is equivalent to the qualification test material.

Key processing changes shall be subject to qualification prior to use of the material produced by the revised process. The Certificate Holder shall determine whether a complete or partial re-qualification program per Section A.8.1.7.6 is required, depending on the characteristics of the material that could be affected by the process change.

A.8.1.7.6.2 Definition of Key Process Changes

Key process changes are those which could adversely affect the uniform distribution of the boron carbide in the aluminum, reduce density, or reduce the mechanical strength or ductility of the MMC.

A.8.1.7.6.3 Identification and Control of Key Process Changes

CAUTION

Section A.8.1.7.6.3 is incorporated by reference into the CoC 9302 Conditions (paragraph tbd) and shall not be deleted or altered in any way without a CoC revision approval from the NRC. The text of this section is shown in bold type to distinguish it from other sections.

The manufacturer shall provide the Certificate Holder with a description of materials and process controls used in producing the MMC. The Certificate Holder and manufacturer shall identify key process changes as defined in Section A.8.1.7.6.2.

An increase in nominal boron carbide content over that previously qualified shall always be regarded as a key process change. The following are examples of other changes that may be established as key process changes, as determined by the Certificate Holder's review of the specific applications and production processes:

- a) **Changes in the boron carbide particle size specification that increase the average particle size by more than 5 microns or that increase the amount of particles larger than 60 microns from the previously qualified material by more than 5% of the total distribution but less than the 10% limit,**
- b) **Change of the billet production process, e.g., from vacuum hot pressing to cold isostatic pressing followed by vacuum sintering,**
- c) **Change in the nominal matrix alloy,**
- d) **Changes in mechanical processing that could result in reduced density of the final product, e.g., for PM or thermal spray MMCs that were qualified with extruded material, a change to direct rolling from the billet,**
- e) **For MMCs using a 6000 series aluminum matrix, changes in the billet formation process that could increase the likelihood of magnesium reaction with the boron carbide, such as an increase in the maximum temperature or time at maximum temperature, and**
- f) **Changes in powder blending or melt stirring processes that could result in less uniform distribution of boron carbide, e.g., change in duration of powder blending.**

In no case shall process changes be accepted if they result in a product outside the limits in Sections A.8.1.7.5.1 and A.8.1.7.5.4.

A.8.1.7.2 Poisson Acceptance for DSCs Already Loaded and DSCs Under Fabrication

CAUTION

Section A.8.1.7.2 is incorporated by reference into the CoC 9302 Conditions (paragraph tbd) and shall not be deleted or altered in any way without a CoC revision approval from the NRC. The text of this section is shown in bold type to distinguish it from other sections.

The neutron absorber acceptance criteria as described in Section A.8.1.7.1 are applicable to all the canister types described elsewhere in this SAR. However, for canister types which are already in service under 10CFR Part72 and/or canister types whose fabrication activities commenced before the approval date of COC 9302 Revision 5, the neutron absorber material acceptance requirements for each specific canister type as described in the applicable 10CFR Part72 approved amendment are applicable.

References:

1. "Aluminum Standards and Data, 2003" The Aluminum Association
2. Natrella, "Experimental Statistics," Dover, 2005

RAI 3-4

Demonstrate by analysis that the personnel barrier is not exposed to hot stream air from the cask shield shell.

Page A.3-38 of the SAR states that since the personnel barrier is far apart from the cask shield shell, it is not exposed to the hot air streams from the cask. The applicant should perform a thermal analysis (e.g., CFD analysis) to demonstrate the validity of this assumption.

This information is needed to determine compliance with 10 CFR Part 71 (71.71)

Draft Response to RAI 3-4

The following discussion will be incorporated into the SAR.

The assumption that the personnel barrier is not exposed to hot air stream from the cask shield shell can be justified by calculation of the thermal boundary layer thickness around the lower half of the cask. This calculation demonstrates that the thermal boundary layer thickness is smaller than the shortest distance between the personnel barrier and the cask and therefore the personnel barrier remains out of the hot air stream from the cask.

The large diameter of the cask and the relative large temperature difference between the cask outer surface and ambient temperature suggest that the free convection over the cylinder is a turbulent flow.

The theoretical and experimental studies of the free convection and its related thermal boundary layer thickness are widely available and well documented (references [3.4-1], [3.4-3], [3.4-4], and [3.4-5]). These correlations can be used to determine the free convection thermal boundary layer thickness over the horizontal MP197HB cask. These studies show that the thickness of the free convection thermal boundary layer is inversely proportional to a power of the local Nusselt number for laminar or turbulent flows.

$$\frac{\delta}{x} = \frac{Cf(\text{Pr})}{\text{Nu}_x^m} \quad (1)$$

- δ = local thermal boundary layer thickness
- x = local position
- $f(\text{Pr})$ = a function of Prandtl number
- Nu_x = local Nusselt number
- m and c = constant values

For instance, the theoretical calculation in reference [3.4-4] determines the following equation for a free convection laminar flow over flat vertical plates.

$$\frac{\delta}{x} = \frac{2}{\text{Nu}_x}$$

This equation means that $c = 2$, $f(\text{Pr}) = 1$, and $m = 1$ in equation (1).

The correlations to determine the free convection thermal boundary layer thickness and local Nusselt number over a vertical flat plate in turbulent flow are documented in references [3.4-2] and [3.4-3]. These correlations are shown below.

$$\frac{\delta_x}{x} = 0.565 \text{Gr}_x^{-0.1} \text{Pr}^{-8/15} \left(1 + 0.494 \text{Pr}^{2/3}\right)^{0.1} \quad [3.4-2] \quad (2)$$

$$\text{Gr}_x = \frac{g\beta\Delta T x^3}{\nu^2}$$

$$\text{Nu}_x = 0.0295 \left[\frac{\text{Pr}^7}{\left(1 + 0.494 \text{Pr}^{2/3}\right)^6} \right]^{1/15} \text{Gr}_x^{2/5} \quad [3.4-3]$$

$$\text{Nu}_L = 0.834 \text{Nu}_x \quad [3.4-3] \quad (3)$$

An examination of the above equations shows that the thermal boundary layer thickness is reversely proportional to the $\text{Nu}_x^{0.25}$ for turbulent free convection over a vertical flat plate.

Considering the relationship between the thermal boundary layer thickness and the local Nusselt number, the boundary layer thickness over a horizontal cylinder in free convection turbulent flow can be determined using the correlations over a vertical flat plate and the inverse ratio of the local Nusselt numbers. Since the correlations for the average Nusselt numbers of free convection for vertical flat plates and horizontal cylinders are known better than the local Nusselt numbers, the ratio of the local Nusselt numbers are extended to include the average Nusselt numbers and avoid elimination of any functions related to Prandtl number.

$$\frac{\delta_{D0}}{\delta_x} = \frac{\delta_L}{\delta_x} \cdot \frac{\delta_D}{\delta_L} \cdot \frac{\delta_{D0}}{\delta_D}$$

$$\frac{\delta_{D0}}{\delta_x} = \left(\frac{\text{Nu}_x}{\text{Nu}_L}\right)^p \left(\frac{\text{Nu}_L}{\text{Nu}_D}\right)^q \left(\frac{\text{Nu}_D}{\text{Nu}_{D0}}\right)^r \quad (4)$$

δ_{D0} = thermal boundary layer thickness at midsection of a horizontal cylinder ($\alpha = 0$)

δ_x = thermal boundary layer thickness at height of x for a vertical flat plate

Nu_x = local Nusselt number for a vertical flat plate at height x

Nu_L = average Nusselt number for a vertical flat plate at height L

Nu_{D0} = local Nusselt number at midsection of a horizontal cylinder ($\alpha = 0$)

Nu_D = average Nusselt number for a horizontal cylinder with outer diameter of D

p , q , and r = constant parameters

Based on the discussion for the thermal boundary layer thickness over a vertical flat plate above, the constant parameter p in equation (4) is 0.25.

An extensive study on free convection over large diameter, horizontal cylinders conducted in reference [3.4-6] shows that the onset of turbulent transition occurs at a point passing the midsection of the cylinder by five degree even for large Rayleigh numbers so that the free convection over the lower half of the cylinder remains laminar.

Since the personnel barrier designed for MP197HB cask is extended only to the midsection of the cask, the correlations for free convection laminar flow over horizontal cylinders can be used to determine the thermal boundary layer thickness at this location.

The free convection local Nusselt number over a horizontal cylinder in laminar flow in air is given in reference [3.4-5] as follows.

$$Nu_{D\alpha} = 0.604 Gr_D^{1/4} \phi(\alpha) \quad [3.4-5]$$

$$Gr_D = \frac{g\beta \Delta T D^3}{\nu^2}$$

α	-90	-60	-30	0	30	60	75	90
$\phi(\alpha)$	0.76	0.75	0.72	0.66	0.58	0.46	0.36	0
	Bottom half			Top half				

The local Nusselt number at the midsection of the cylinder at $\alpha = 0$ is:

$$Nu_{D0} = 0.604 Gr_D^{1/4} \times 0.66$$

Based on the above correlation, the average Nusselt number over the horizontal cylinder is:

$$Nu_D = \frac{1}{180} \int_{-90}^{90} Nu_{D\alpha} d\alpha = 0.604 Gr_D^{1/4} \times \frac{1}{180} \int_{-90}^{90} \phi(\alpha) d\alpha$$

The integration of $\phi(\alpha)$ over the range of -90° to 90° performed using the data in the above table gives:

$$Nu_D = 0.604 Gr_D^{1/4} \times 0.6025$$

Comparison of the correlations for Nu_{D0} and Nu_D gives:

$$Nu_D = \frac{0.6025}{0.66} Nu_{D0} = 0.913 Nu_{D0} \quad (5)$$

Since the equation (5) is based on free convection laminar flow, the constant parameter r in equation (4) is equal to 1.

The ratio of the average Nusselt numbers for vertical flat plate and horizontal cylinder can be determined using the corresponding correlations shown in Section A.3.3.1.1.

The thickness of the boundary layer at the midsection of the cask can be determined by substitution of the correlations for the local and average Nusselt numbers into equation (4). The height (L) of the vertical flat plate can be set equal to the outer diameter of the cask (D) for this evaluation. Average of the cask outer surface and ambient temperatures are considered in calculation of the Nusselt numbers.

As seen above, the correlations for the local and average Nusselt numbers depend on the Grashof and Prandtl numbers, which in turn depend on the cask outer surface temperature. A

sensitivity analysis is performed to cover the effects of a wide range of cask temperatures from 200°F to 500°F on the thickness of free convection thermal boundary layer at the midsection of the cask. This sensitivity analysis starts with variation of Grashof and Prandtl numbers as summarized in the following table.

Variation of Grashof, Prandtl, and Rayleigh Numbers

$T_{\infty} = 100^{\circ}\text{F}$

For $L=D$

T_{cask}	T_{cask}	T_{∞}	T_{avg}	β	ν	Gr	Pr	Ra
(F)	(K)	(K)	(K)	(1/K)	(m^2/s)	(---)	(---)	(---)
200	367	311	339	2.95E-03	2.235E-05	4.931E+10	0.71	3.490E+10
300	422	311	367	2.73E-03	2.849E-05	5.609E+10	0.70	3.948E+10
400	478	311	394	2.54E-03	3.516E-05	5.135E+10	0.70	3.602E+10
500	533	311	422	2.37E-03	4.232E-05	4.415E+10	0.70	3.091E+10

The values in the above table are calculated based on air properties shown in the SAR, Section A.3.2.1, Item 16, at the average air temperature. As seen in the above table, the Grashof number varies between 5.6E10 and 4.4E10, the Prandtl number varies between 0.70 and 0.71, and the Rayleigh number varies between 3.1E10 and 4.0E10 for the cask outer surface temperatures between 200°F and 500°F. Since the variation of Prandtl is relative small, an average Prandtl number of 0.70 is considered in the sensitivity analysis to calculate the average Nusselt numbers for a vertical flat plate (Nu_L) and a horizontal cylinder (Nu_D). To bound the variation of the Rayleigh number conservatively, the average Nusselt numbers Nu_L and Nu_D are evaluated for a wider range between 1E10 and 1E11.

As shown in the SAR, Section A.3.3.1.1, the correlation for Nu_L depends on C_t^y and f factors, which in turn depend on Prandtl number and surface temperature, respectively. C_t^y is a weak function of Prandtl number. The variation of the f factor is determined for a cask outer surface temperature from 200°F to 500°F. The variations of these values are summarized in the following table.

Variation of C_t^y and f in Calculation of Nu_L

$T_{\infty} = 100^{\circ}\text{F}$

Pr	C_t^y	T_{cask}	f
(---)	(---)	(°F)	(---)
0.70	0.103	200	1.014
0.71	0.103	300	1.028
Average	0.103	400	1.042
		500	1.056
		Average	1.035

The average values of C_t^y and f from the above table are considered in calculation of Nu_L . The variation of the average Nusselt numbers Nu_L and Nu_D and their ratios summarized in the table below.

Variation of Nu_L/Nu_D

Vertical Flat Plate

Pr = 0.70

Ra	Nu^T	Nu_l	C_t^V	f	Nu_t	Nu_L
(---)	(---)	(---)	(---)	(---)	(---)	
1.00E+10	162.86	163.9	0.103	1.035	208.5	216.0
2.00E+10	193.67	194.7	0.103	1.035	275.0	280.5
5.00E+10	243.53	244.5	0.103	1.035	384.0	388.1
8.00E+10	273.89	274.9	0.103	1.035	452.4	456.1
1.00E+11	289.61	290.6	0.103	1.035	488.5	492.0

Horizontal Cylinder

Pr = 0.70

Ra	Nu^T	F	Nu_l	\bar{C}_t	Nu_t	Nu_D	Nu_L/Nu_D
(---)	(---)	(---)	(---)	(---)	(---)	(---)	(---)
1.00E+10	125.73	0.940	126.7	0.103	221.9	222.0	0.973
2.00E+10	149.51	0.942	150.5	0.103	279.6	279.6	1.003
5.00E+10	188.00	0.944	188.9	0.103	379.5	379.5	1.023
8.00E+10	211.44	0.945	212.4	0.103	443.8	443.8	1.028
1.00E+11	223.58	0.945	224.5	0.103	478.1	478.1	1.029
Average							1.011

As shown in the above table, the ratio of Nu_L to Nu_D varies between 0.973 and 1.029 for the range of considered Rayleigh numbers. An average value of 1.011 is considered for this ratio to use in equation (4). Since this ratio is close to one, the constant parameter q in equation (4) does not have any significant effect and can be omitted.

Substitution of the local and average Nusselt number ratios from equation (3), equation (5), and the table of Nu_L/Nu_D variations into equation (4) gives:

$$\delta_{D0} = (1/0.834)^{0.25} \times 1.011 \times 0.913 \delta_x$$

Using δ_x from equation (2) in the above equation determines the range of boundary layer thickness at the midsection of the cask as summarized in the following table.

Thickness of the Thermal Boundary Layer

$T_\infty = 100^\circ\text{F}$

$L = D = 97.75''$

T_{cask}	T_{cask}	T_∞	T_{avg}	Gr	Pr	δ_x/L	δ_x	δ_{D0}
(°F)	(K)	(K)	(K)	(---)	(---)	(---)	(in)	(in)
200	367	311	339	4.931E+10	0.71	0.060	5.9	5.7
300	422	311	367	5.609E+10	0.70	0.059	5.8	5.6
400	478	311	394	5.135E+10	0.70	0.060	5.9	5.7
500	533	311	422	4.415E+10	0.70	0.061	6.0	5.7

As seen in the above table, the variation of the thermal boundary layer thickness is small and its maximum value at the midsection of the cask is 5.7'' for a uniform cask surface temperature of

500°F. Based on data shown in the SAR, Section A.3.3.1.2, the shortest distance between the outer surface of the cask and the personnel barrier is over 9”.

Shortest distance = distance to cask centerline – cask OD/2 = 58 – 97.75 / 2 = 9.125”

The conservatively evaluated boundary layer thickness of 5.7” is much smaller than shortest distance between the outer surface of the cask and the personnel barrier. Therefore, the personnel barrier remains out of the hot air streams flowing around the cask outer surface.

References for Draft Response to RAI 3-4

- 3.4-1. Eckert, “Introduction to the Transfer of Heat and Mass”, 1st Edition, 1950.
- 3.4-2. Eckert and Jackson, “Analysis of Turbulent Free-Convection Boundary Layer on Flat Plate“, NASA Technical Reports, Report Number NACA-TN-2207, 1950.
- 3.4-3. Kays, Crawford, and Weigand, “Convective Heat and Mass Transfer”, 4th Edition, 2005.
- 3.4-4. Holman, “Heat Transfer”, 8th Edition, 1997.
- 3.4-5. Kreith, “Principles of Heat Transfer”, 3rd Edition, 1973.
- 3.4-6. Misumi, Suzuki, and Kitamura, “Fluid Flow and Heat Transfer of Natural Convection around Large Horizontal Cylinders: Experiments with Air”, *Heat Transfer –Asian Research*, 32 (4), 2003.

Note: For the convenience of reviewers, excerpts from some of these references are also included in this handout, on the next 21 pages. That information will not be incorporated into the SAR.

From SGreen@swri.edu Thu Feb 22 09:14:46 1996
 To: <ph@gramercy.ios.com>
 Subject: Solar Collector Test Cell

email with excerpts from Eckert, Ref. 3.4-2

I have had a chance to look at your write-up and the data for your solar collector test. You have used the term 'structured convection' in this write-up to describe the heat transfer process in the collector as some new phenomenon. You have said that it is at least different from 'normal turbulent convection'. In fact, the heat transfer process in place during most of the time that the data are gathered is simple natural convection that is described in most engineering heat transfer textbooks.

We could develop a mathematical model using computational fluid dynamics for your test cell, but I'm not sure that it will tell us anything really new about the flow field. The data you provided, including the smoke pattern description and the 'anomaly', can all be described by a rough engineering analysis. What follows is such a first-order assessment of the data based on my interpretation of the test setup.

For natural convection from a vertical surface, only the fluid close to the surface moves under the effect of buoyancy forces caused by the decreased fluid density with respect to the fluid farther away from the surface. The fluid in contact with the wall is stationary and the fluid far away from the wall is approximately stationary. In the region just off the wall, however, the fluid reaches a maximum velocity but decreases to zero at the wall and far away from the wall. While the exact fluid velocity can be obtained by a numerical solution to the appropriate differential equations, an equation which closely approximates the velocity profile for turbulent flow is given as

$$u/u_{max} = 1/0.537 * (y/d)^{(1/7)} * (1-y/d)^4$$

where u = local velocity parallel to the wall, u_{max} = maximum velocity in the profile, y = distance from the wall, d = local total boundary layer thickness. By differentiating this equation, we can see that the maximum velocity occurs at about 3.5% of the boundary layer thickness away from the wall. When expressed this way (i.e., dimensionless), the velocity profile is independent of the position along the wall.

The boundary layer thickness and the maximum velocity are both functions of the distance along the wall. These have been reported in the literature by a number of workers, but the solution of Eckert and Jackson (NACA TN 2207, 1950) is still a good approximation:

$$u_{max} = 0.636 * \mu/x * (Gr)^{(1/2)} * (1+0.494*Pr^{(2/3)})^{(-1/2)}$$

$$d = 0.565 * x * Gr^{(-1/10)} * Pr^{(-8/15)} * (1+0.494*Pr^{(2/3)})^{(1/10)}$$

where x = distance up the wall from the bottom, μ = fluid dynamic viscosity, Gr = Grashof Number (a heat transfer parameter), Pr = fluid Prandtl Number

We can use these relationships to get an idea of the velocity and the boundary layer thickness in your collector. From the graphs near noon, I estimate that the wall temperature is 180 F and the air temperature is 100 F at a position about halfway up the wall, which I assume is about 6 ft total height, from these temperatures, the following air properties are taken from a handbook:

[PFH ed. Note: measurements were taken at ~3 ft height]

	100 F	180 F	mean value	
density =	0.071	0.062	0.067	lb/ft ³
viscosity =	1.285*10 ⁻⁵	1.409*10 ⁻⁵	1.347*10 ⁻⁵	lb/ft*sec
B =	1.79*10 ⁻³	1.57*10 ⁻³	1.68*10 ⁻³	1/F (thermal expansion coefficient)
Pr =	0.72	0.72	0.72	

The Grashof Number, a natural convection heat transfer parameter is

$$Gr = (\text{density})^2 * g * B / \mu^2 * (T_{\text{wall}} - T_{\text{air}}) * x^3$$

email with excerpts from Eckert, Ref. 3.4-2

Using the arithmetic mean of the properties, the Grashof Number (a dimensionless value) is

$$Gr = 2.89 * 10^9$$

The $Gr * Pr$ product is known as the Rayleigh Number, $Ra = Gr * Pr = 2.08 * 10^9$ for this case. If the Rayleigh Number is greater than $1 * 10^9$, the flow is turbulent; so the use of the above equations is warranted. The boundary layer thickness and the maximum velocity are now computed for this position along the wall as $d = 2.9$ " and $u_{\text{max}} = 1.9$ ft/sec, respectively. The maximum velocity is found at 0.1" from the wall.

[PFH ed. Note: observed $d < 1/2$ ", observed $u_{\text{max}} \sim 15$ ft/sec]

This explains the nature of your smoke patterns. The fluid is relatively quiescent at distances greater than 3" from the wall, but the velocity increases to almost 2 ft/sec near the surface. The layer of fluid moving near the wall 'pulls' fluid from the bulk so that the boundary layer thickens as it moves up the heated wall. This value of Ra is only 2 times the value for laminar-turbulent transition; so the flow is not strongly turbulent. This is evidenced by the wavy pattern of the smoke as opposed to a more chaotic smoke pattern.

The heated fluid spills over the top of the absorber and is replaced by cooler fluid entering at the bottom, thereby setting up a circulating flow in the container - mostly up in the air space along the absorber, mostly down through the rock storage. Because of the limited capacity of the rock storage, the top of the rock pile is heated to such a temperature late in the day that the driving force for flow up the storage is nearly as strong as for flow up the wall. In that case the, air will circulate only within the space in front of the absorber which will rapidly heat the volume of air between the glass and the absorber. This is indicated in the data. When the air is heated to a high enough temperature, or the rock pile cools sufficiently, the normal circulation pattern is re-established.

I hope this assessment is useful to you. If necessary, I can expand it and make it more formal, but I will have to charge you for that type of effort.

Steve Green
Southwest Research Institute
210-522-3519
sgreen@swri.edu

□□□□□□

Excerpts from Kays,
Ref. 3.4-3

from the constant-property solutions. An analogous conclusion was obtained for the laminar forced-convection boundary layer in Chap. 15.

Sparrow and Gregg¹⁴ obtained numerical solutions for a number of other hypothetical fluid-property variations. They included $\mu \propto T^{3/4}$ and $k \propto T^{3/4}$, which is close to the 0.8-power law for gases in the moderate temperature range. The major conclusion from their work was that a *reference temperature* could satisfactorily be used to correct the constant-property solutions. They proposed that all properties in the constant-property correlations be evaluated at a reference temperature

$$T_R = T_s - 0.38(T_s - T_\infty) \quad (17-43)$$

For gases they recommend $\beta = 1/T_\infty$ and for low Pr fluids $\beta = 1/T_R$. Later Miyamoto⁵⁰ investigated the effect of variable properties on heat transfer for laminar gas flows along a vertical flat plate. He assumed that the fluid properties are such that $\rho \propto T^{-1}$, $\mu \propto T^\omega$ and $k \propto T^\omega$. Specific heat was assumed to be constant. He suggested for Pr = 0.7 the use of the reference temperature

$$T_R = T_\infty + 0.73(T_s - T_\infty) = T_s - 0.27(T_s - T_\infty) \quad (17-44)$$

for $\omega = 3/4$, $-0.3 < (T_s - T_\infty)/T_\infty < 3$. If the fluid properties are evaluated according to Eq. (17-44), Miyamoto⁵⁰ found that the effect of variable properties could satisfactorily be corrected and the constant property solutions can be used. However, almost all Nu_x data and data correlation reported in the open literature, and in this chapter, are formulated using $T_R = 0.5(T_s + T_\infty)$, the average film temperature. For the heat-flux boundary condition, T_R is an unknown. To evaluate Gr_x and Nu_x , the wall temperature must be guessed and iterated until the T_s used in T_R is the same as that calculated from \dot{q}_s'' and Nu_x .

TURBULENT FLOW ON A VERTICAL AND SEMI-INFINITE FLAT PLATE

After a certain distance from the leading edge of the vertical plate, the boundary layer becomes unstable. This can be observed in Fig. 17-4, which is a photograph taken with a Mach-Zehnder interferometer by Eckert and Soehngen.⁴⁶ The numbers shown in Fig. 17-4 indicate the distance from the leading edge of the plate in inches. It can be observed that as the boundary layer becomes unstable, waves appear, which increase in amplitude for larger distances. Finally, the waves transform into turbulence, which is shown on the photograph in Fig. 17-4.

An early analysis for the turbulent boundary layer was carried out by Eckert and Jackson¹⁶ using precisely the same technique that Eckert¹³ used for laminar free-convection flow. Equations (17-39) and (17-40) are again applicable. According to available experimental velocity and temperature profile data, the profile shapes used by Eckert and Jackson were

$$\frac{u}{U} = \left(\frac{y}{\delta}\right)^{1/7} \left(1 - \frac{y}{\delta}\right)^4$$

$$\frac{T - T_\infty}{T_s - T_\infty} = 1 - \left(\frac{y}{\delta}\right)^{1/7}$$

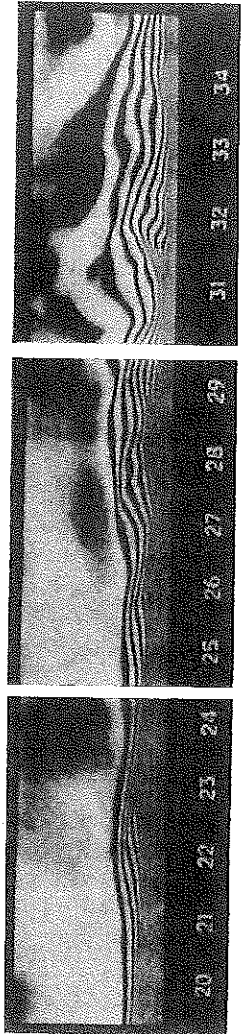


Figure 17-4
Interference photograph of transition to turbulence at a vertical flat plate after Eckert and Soehngen.⁴⁶

In these profile shapes U is a characteristic velocity, T_s is constant, and δ is the outer edge of the boundary layer. Note that differentiating the velocity profile gives $u_{\max} = 0.537U$. Thus U is defined to eliminate the constant obtained in curve-fitting the experimental velocity profile data.

To solve the integral equations, the laws for wall shear stress and heat flux need to be modeled. Eckert and Jackson argued that in the near-wall region τ_s would be similar to that for forced convection. The shear-stress law they used follows from the power-law form of the wall law for the near-wall region, Eq. (11-17). Because $u = 0$ at $y = \delta$, Eckert and Jackson used the characteristic velocity U in place of u_∞ at $y = \delta$. The resulting equation for the shear stress becomes

$$\tau_s = 0.0225\rho U^2 \left(\frac{\nu}{U\delta}\right)^{1/4}$$

The wall heat flux is obtained by using an analogy between momentum and heat transfer with a Prandtl number function for fluids with Prandtl numbers near unity:

$$St = \frac{\dot{q}_s''}{\rho c U (T_s - T_\infty)} = 0.0225 \left(\frac{\nu}{U\delta}\right)^{1/4} Pr^{-2/3}$$

Solution for the turbulent case follows exactly the solution procedure for the laminar case. The profiles and expressions for τ_s and \dot{q}_s'' are substituted into Eqs. (17-39) and (17-40). This results in two ordinary differential equations for U and δ . The equations are solved by assuming the power-law functions

$$U = C_u x^m, \quad \delta = C_\delta x^n$$

These functions are substituted into the differential equations, and the exponents and constants are obtained directly. The resulting Nusselt number is found to be

$$Nu_x = 0.0295 \left[\frac{Pr^7}{(1 + 0.494 Pr^{2/3})^6} \right]^{1/15} Gr_x^{2/5} \quad (17-45)$$

This analysis suggests that h varies as $x^{0.2}$. To obtain an average heat-transfer coefficient, we follow the same procedure used with Eq. (17-34) for the laminar solution, which leads to

$$Nu = 0.834 Nu_x$$

Bailey¹⁷ carried out a turbulent integral analysis using Eqs. (17-39) and (17-40) and the same velocity profile and τ_s expression as Eckert and Jackson. For the temperature profile, and therefore \dot{q}_s'' , Bailey used a two-layer temperature model with a laminar sublayer out to $y^+ = 15$ and then a constant-diffusivity turbulent region. He found that

$$\begin{aligned} Pr = 0.73, & \quad Nu_x = 0.10 (Gr_x Pr)^{1/3} \\ Pr = 0.01, & \quad Nu_x = 0.060 Gr_x^{1/4} \end{aligned} \quad (17-46)$$

7

Natural Convection Systems

7-1 INTRODUCTION

Our previous discussions of convection heat transfer have considered only the calculation of forced-convection systems where the fluid is forced by or through the heat-transfer surface. Natural, or free, convection is observed as a result of the motion of the fluid due to density changes arising from the heating process. A hot radiator used for heating a room is one example of a practical device which transfers heat by free convection. The movement of the fluid in free convection, whether it is a gas or a liquid, results from the buoyancy forces imposed on the fluid when its density in the proximity of the heat-transfer surface is decreased as a result of the heating process. The buoyancy forces would not be present if the fluid were not acted upon by some external force field such as gravity, although gravity is not the only type of force field which can produce the free-convection currents; a fluid enclosed in a rotating machine is acted upon by a centrifugal force field, and thus could experience free-convection currents if one or more of the surfaces in contact with the fluid were heated. The buoyancy forces which give rise to the free-convection currents are called *body forces*.

7-2 FREE-CONVECTION HEAT TRANSFER ON A VERTICAL FLAT PLATE

Consider the vertical flat plate shown in Fig. 7-1. When the plate is heated, a free-convection boundary layer is formed, as shown. The velocity profile in this boundary layer is quite unlike the velocity profile in a forced-convection boundary layer. At the wall the velocity is zero because of the no-slip condition; it increases to some maximum value and then decreases to zero at the edge of the boundary layer since

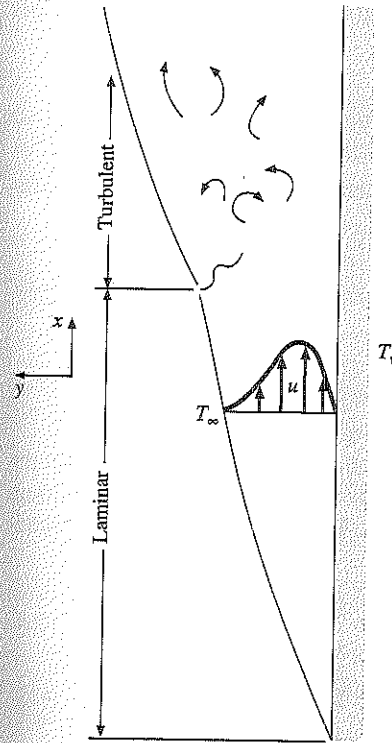


FIG. 7-1 Boundary layer on a vertical flat plate.

the “free-stream” conditions are at rest in the free-convection system. The initial boundary-layer development is laminar; but at some distance from the leading edge, depending on the fluid properties and the temperature difference between wall and environment, turbulent eddies are formed, and transition to a turbulent boundary layer begins. Farther up the plate the boundary layer may become fully turbulent.

To analyze the heat-transfer problem, we must first obtain the differential equation of motion for the boundary layer. For this purpose we choose the x coordinate along the plate and the y coordinate perpendicular to the plate as in the analyses of Chap. 5. The only new force which must be considered in the derivation is the weight of the element of fluid. As before, we equate the sum of the external forces in the x direction to the change in momentum flux through the control volume $dx dy$. There results

$$\rho \left(u \frac{\partial u}{\partial x} + v \frac{\partial u}{\partial y} \right) = - \frac{\partial p}{\partial x} - \rho g + \mu \frac{\partial^2 u}{\partial y^2} \quad (7-1)$$

where the term $-\rho g$ represents the weight force exerted on the element. The pressure gradient in the x direction results from the change in elevation up the plate. Thus

$$\frac{\partial p}{\partial x} = -\rho \infty g \quad (7-2)$$

Excerpts from Holman, Ref. 3.4-4

Handout for NRC Meeting with Transnuclear, February 22, 2010

In other words, the change in pressure over a height dx is equal to the weight per unit area of the fluid element. Substituting Eq. (7-2) into Eq. (7-1) gives

$$\rho \left(u \frac{\partial u}{\partial x} + v \frac{\partial u}{\partial y} \right) = g(\rho_\infty - \rho) + \mu \frac{\partial^2 u}{\partial y^2} \quad (7-3)$$

The density difference $\rho_\infty - \rho$ may be expressed in terms of the volume coefficient of expansion β , defined by

$$\beta = \frac{1}{V} \left(\frac{\partial V}{\partial T} \right)_p = \frac{1}{V_\infty} \frac{V - V_\infty}{T - T_\infty} = \frac{\rho_\infty - \rho}{\rho(T - T_\infty)}$$

so that

$$\rho \left(u \frac{\partial u}{\partial x} + v \frac{\partial u}{\partial y} \right) = g\rho\beta(T - T_\infty) + \mu \frac{\partial^2 u}{\partial y^2} \quad (7-4)$$

This is the equation of motion for the free-convection boundary layer. Notice that the solution for the velocity profile demands a knowledge of the temperature distribution. The energy equation for the free-convection system is the same as that for a forced-convection system at low velocity:

$$\rho c_p \left(u \frac{\partial T}{\partial x} + v \frac{\partial T}{\partial y} \right) = k \frac{\partial^2 T}{\partial y^2} \quad (7-5)$$

The volume coefficient of expansion β may be determined from tables of properties for the specific fluid. For ideal gases it may be calculated from (see Prob. 7-3)

$$\beta = \frac{1}{T}$$

where T is the absolute temperature of the gas.

Even though the fluid motion is the result of density variations, these variations are quite small, and a satisfactory solution to the problem may be obtained by assuming incompressible flow, that is, $\rho = \text{constant}$. To effect a solution of the equation of motion, we use the integral method of analysis similar to that used in the forced-convection problem of Chap. 5. Detailed boundary-layer analyses have been presented in Refs. 13, 27, and 32.

For the free-convection system, the integral momentum equation becomes

$$\begin{aligned} \frac{d}{dx} \left(\int_0^\delta \rho u^2 dy \right) &= -\tau_w + \int_0^\delta \rho g \beta (T - T_\infty) dy \\ &= -\mu \left. \frac{\partial u}{\partial y} \right|_{y=0} + \int_0^\delta \rho g \beta (T - T_\infty) dy \end{aligned} \quad (7-6)$$

and we observe that the functional form of both the velocity and the temperature distributions must be known in order to arrive at the solution. To obtain these functions, we proceed in much the same way as in Chap. 5. The following conditions apply for the temperature distribution:

$$T = T_w \quad \text{at } y = 0$$

$$T = T_\infty \quad \text{at } y = \delta$$

$$\frac{\partial T}{\partial y} = 0 \quad \text{at } y = \delta$$

so that we obtain for the temperature distribution

$$\frac{T - T_\infty}{T_w - T_\infty} = \left(1 - \frac{y}{\delta} \right)^2 \quad (7-7)$$

Three conditions for the velocity profile are

$$u = 0 \quad \text{at } y = 0$$

$$u = 0 \quad \text{at } y = \delta$$

$$\frac{\partial u}{\partial y} = 0 \quad \text{at } y = \delta$$

An additional condition may be obtained from Eq. (7-4) by noting that

$$\frac{\partial^2 u}{\partial y^2} = -g\beta \frac{T_w - T_\infty}{\nu} \quad \text{at } y = 0$$

As in the integral analysis for forced-convection problems, we assume that the velocity profiles have geometrically similar shapes at various x distances along the plate. For the free-convection problem, we now assume that the velocity may be represented as a polynomial function of y multiplied by some arbitrary function of x . Thus,

$$\frac{u}{u_x} = a + by + cy^2 + dy^3$$

where u_x is a fictitious velocity which is a function of x . The cubic-polynomial form is chosen because there are four conditions to satisfy, and this is the simplest type of function which may be used. Applying the four conditions to the velocity profile listed above, we have

$$\frac{u}{u_x} = \frac{\beta \delta^2 g (T_w - T_\infty) y}{4u_x \nu} \left(1 - \frac{y}{\delta} \right)^2$$

The term involving the temperature difference, δ^2 , and u_x may be incorporated into the function u_x so that the final relation to be assumed for the velocity profile is

$$\frac{u}{u_x} = \frac{y}{\delta} \left(1 - \frac{y}{\delta} \right)^2 \quad (7-8)$$

A plot of Eq. (7-8) is given in Fig. 7-2. Substituting Eqs. (7-7) and (7-8) into Eq. (7-6) and carrying out the integrations and differentiations yields

$$\frac{1}{105} \frac{d}{dx} (u_x^2 \delta) = \frac{1}{3} g \beta (T_w - T_\infty) \delta - \nu \frac{u_x}{\delta} \quad (7-9)$$

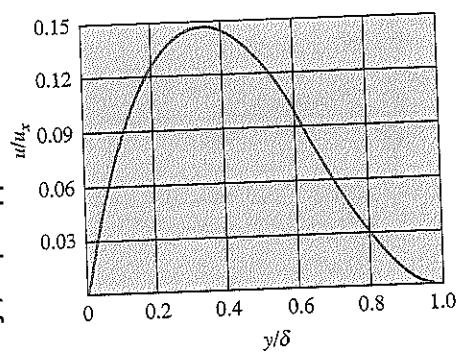


FIG. 7-2
Free-convection velocity profile given by Eq. (7-8).

Handout for NRC Meeting with Transnuclear, February 22, 2010

The integral form of the energy equation for the free-convection system is

$$\frac{d}{dx} \left[\int_0^\delta u(T - T_\infty) dy \right] = -\alpha \left. \frac{dT}{dy} \right|_{y=0} \quad (7-10)$$

and when the assumed velocity and temperature distributions are inserted into this equation and the operations are performed, there results

$$\frac{1}{30} (T_w - T_\infty) \frac{d}{dx} (u_x \delta) = 2\alpha \frac{T_w - T_\infty}{\delta} \quad (7-11)$$

It is clear from the reasoning which led to Eq. (7-8) that

$$u_x \sim \delta^2 \quad (7-12)$$

Inserting this type of relation in Eq. (7-9) yields the result that

$$\delta \sim x^{1/4} \quad (7-13)$$

We therefore assume the following exponential functional variations for u_x and δ :

$$u_x = C_1 x^{1/2} \quad (7-14)$$

$$\delta = C_2 x^{1/4} \quad (7-15)$$

Introducing these relations into Eqs. (7-9) and (7-11) gives

$$\frac{5}{420} C_1^2 C_2 x^{1/4} = g\beta(T_w - T_\infty) \frac{C_2}{3} x^{1/4} - \frac{C_1}{C_2} \nu x^{1/4} \quad (7-16)$$

and
$$\frac{1}{40} C_1 C_2 x^{-1/4} = \frac{2\alpha}{C_2} x^{-1/4} \quad (7-17)$$

These two equations may be solved for the constants C_1 and C_2 to give

$$C_1 = 5.17 \nu \left(\frac{20}{21} + \frac{\nu}{\alpha} \right)^{-1/2} \left[\frac{g\beta(T_w - T_\infty)}{\nu^2} \right]^{1/2} \quad (7-18)$$

$$C_2 = 3.93 \left(\frac{20}{21} + \frac{\nu}{\alpha} \right)^{1/4} \left[\frac{g\beta(T_w - T_\infty)}{\nu^2} \right]^{-1/4} \left(\frac{\nu}{\alpha} \right)^{-1/2} \quad (7-19)$$

The resultant expression for the boundary-layer thickness is

$$\frac{\delta}{x} = 3.93 \text{Pr}^{-1/2} (0.952 + \text{Pr})^{1/4} \text{Gr}_x^{-1/4} \quad (7-20)$$

where the Prandtl number $\text{Pr} = \nu/a$ has been introduced along with a new dimensionless group called the *Grashof number* Gr_x :

$$\text{Gr}_x = \frac{g\beta(T_w - T_\infty)x^3}{\nu^2} \quad (7-21)$$

The heat-transfer coefficient may be evaluated from

$$q_w = -kA \left. \frac{dT}{dy} \right|_w = hA(T_w - T_\infty)$$

Using the temperature distribution of Eq. (7-7), one obtains

$$h = \frac{2k}{\delta} \quad \text{or} \quad \frac{hx}{k} = \text{Nu}_x = 2 \frac{x}{\delta}$$

so that the dimensionless equation for the heat-transfer coefficient becomes

$$\text{Nu}_x = 0.508 \text{Pr}^{1/2} (0.952 + \text{Pr})^{-1/4} \text{Gr}_x^{1/4} \quad (7-22)$$

Equation (7-22) gives the variation of the local heat-transfer coefficient along the vertical plate. The average heat-transfer coefficient may then be obtained by performing the integration

$$\bar{h} = \frac{1}{L} \int_0^L h_x dx \quad (7-23)$$

For the variation given by Eq. (7-22), the average coefficient is

$$\bar{h} = \frac{4}{3} h_{x=L} \quad (7-24)$$

The Grashof number may be interpreted physically as a dimensionless group representing the ratio of the buoyancy forces to the viscous forces in the free-convection flow system. It has a role similar to that played by the Reynolds number in forced-convection systems and is the primary variable used as a criterion for transition from laminar to turbulent boundary-layer flow. For air in free convection on a vertical flat plate, the critical Grashof number has been observed by Eckert and Soehngen [1] to be approximately 4×10^8 . Values ranging between 10^8 and 10^9 may be observed for different fluids and environment "turbulence levels."

A very complete survey of the stability and transition of free-convection boundary layers has been given by Gebhart et al. [13-15].

The foregoing analysis of free-convection heat transfer on a vertical flat plate

in the turbulent range, Gr_L from 2×10^7 to 3×10^{10} , and

Excerpts from Kreith,
Ref. 3.4-5

$$\overline{Nu}_L = \frac{\bar{h}_c L}{k} = 0.54 (Gr_L Pr)^{1/4} \quad (7-22)$$

in the laminar range, Gr_L from 10^5 to 2×10^7 , where L is length of the side of the square. For heated plates facing downward and cooled plates facing upward, the equation

$$\overline{Nu}_L = \frac{\bar{h}_c L}{k} = 0.27 (Gr_L Pr)^{1/4} \quad (7-23a)$$

is recommended (9) in the laminar range, (i.e., Gr from 3×10^5 to 3×10^{10}). Data in the turbulent range are lacking. As a first approximation, the foregoing three equations can be applied to horizontal circular disks if L is replaced by $0.9 D$, where D is the diameter of the disk, and to rectangular surfaces if L is taken as the mean between the two sides.

Experimental data for a cooled circular horizontal plate facing down in a liquid metal are correlated by the relation (29)

$$\overline{Nu}_D = \frac{\bar{h}_c D}{k} = 0.26 (Gr_D Pr^2)^{0.35} \quad (7-23b)$$

Horizontal cylinders, spheres, and cones. The temperature field around a horizontal cylinder heated in air is illustrated in Fig. 7-7, which shows interference fringes photographed by Eckert and Soehngen (7). The flow is laminar over the entire surface. The closer spacing of the interference fringes over the lower portion of the cylinder indicates a steeper temperature gradient and consequently a larger local unit-surface conductance than over the top portion. The variation of the surface conductance with angular position α is shown in Fig. 7-8 for two Grashof numbers. The experimental results do not differ appreciably from the theoretical calculations of Herman (4) who derived the equation

$$Nu_{D\alpha} = 0.604 Gr_D^{1/4} \phi(\alpha) \quad (7-24)$$

for air, i.e., $Pr = 0.74$. The angle α is measured from the horizontal position and numerical values of the function $\phi(\alpha)$ are as follows:

α	-90	-60	-30	0	30	60	75	90
$\phi(\alpha)$	0.76	0.75	0.72	0.66	0.58	0.46	0.36	0
	Bottom half				Top half			

An equation for the average heat-transfer coefficient from single horizontal wires or pipes in free convection, recommended by McAdams (9)

Fluid Flow and Heat Transfer of Natural Convection Around Large Horizontal Cylinders: Experiments with Air

Toshiyuki Misumi,¹ Koji Suzuki,² and Kenzo Kitamura²

¹Department of Mechanical Engineering, Kagoshima National College of Technology, Japan

²Department of Mechanical Engineering, Toyohashi University of Technology, Japan

Natural convective flows of air around large horizontal cylinders were investigated experimentally. The main concerns were the turbulent transition mechanisms and the heat transfer characteristics of turbulent flows. The cylinders were heated with uniform heat flux and their diameters were varied from 200 to 1200 mm to enable experiments over a wide range of modified Rayleigh numbers, $Ra_D^* = 1.0 \times 10^8$ to 5.5×10^{11} . The flow fields around the cylinders were visualized with smoke to investigate the turbulent transition mechanisms. The results show that three-dimensional flow separations occur first at the trailing edge of the cylinder when Ra_D^* exceeds 3.5×10^9 , and the separation points shift upstream with increasing Rayleigh numbers. These separations become a trigger to the turbulent transition and transitional and turbulent flows appear downstream of the separations at higher Rayleigh numbers. However, they occupy a relatively small portion of the cylinder surfaces even at the maximum Rayleigh numbers of the present experiments. The local heat transfer coefficients were also measured. The results show that the coefficients are increased significantly in the transitional and turbulent regions compared with the laminar coefficients. Moreover, the present results for air were compared with previous results for water and the effects of Prandtl number on the flow and heat transfer were discussed. © 2003 Wiley Periodicals, Inc. *Heat Trans Asian Res*, 32(4): 293–305, 2003; Published online in Wiley InterScience (www.interscience.wiley.com). DOI 10.1002/htj.10080

Key words: heat transfer, natural convection, flow visualization, separation, turbulent transition, horizontal cylinder

1. Introduction

Natural convective flows around heated, horizontal cylinders are encountered in many technological applications. These applications have motivated a considerable body of research on their flow and heat transfer characteristics. However, the main concerns of previous studies were directed to laminar natural convection, while relatively less attention was paid to turbulent natural convection. This is partly because turbulent flows are realized only around large cylinders and that the experiments using such cylinders are difficult to perform in a laboratory framework. The lack of experimental data has also hampered the analytical investigations on the turbulent natural convection around cylinders.

© 2003 Wiley Periodicals, Inc.

Despite these circumstances, several workers have carried out experiments on turbulent natural convection. However, most of them measured overall heat transfer coefficients from isothermal cylinders. Summarizing these data, several sets of empirical or semiempirical correlation equations have been proposed. However, these results on the overall heat transfer will not provide basic insight into the flow and temperature fields around the cylinders. On the other hand, the following two works investigated the flow and temperature fields of the turbulent natural convection over heated cylinders. One is the analytical work by Farouk and Guceri [1] and the other is the experimental work by Hattori [2]. Farouk and Guceri first applied the k - ϵ model to the turbulent natural convection of air, and calculated distributions of velocity, temperature, and turbulent kinetic energy around the cylinders. However, their results show considerable differences from the experimental results of Hattori [2], particularly in the local Nusselt numbers and also on the conditions of turbulent transition. Hattori [2] measured the time-averaged velocities and the turbulent quantities such as Reynolds shear stress and turbulent heat flux within the turbulent boundary layers of air. However, the measurements were performed at limited locations over a cylinder in the narrow range of Rayleigh numbers from 3×10^9 to 10^{10} . Therefore, the results will provide little information on the turbulent transition mechanisms and also on the turbulent transport around the cylinder.

Reviewing these studies, we can point out that several subjects remain unsolved. One such subject is related to a turbulent transition. We cannot answer the questions of where and how the turbulent transition takes place over cylinders, and what kind of parameters affects the transition. Moreover, the transition from laminar to turbulent flows will exert significant influences on the local heat transfer characteristics. However, few data are available on the local heat transfer coefficients of large cylinders.

Taking account of the above, the present authors carried out intensive experiments in a previous study [3]. In order to obtain comprehensive knowledge on the flow and temperature fields around cylinders, the flows over the cylinder and the surface temperatures of the cylinders were visualized using dye and liquid crystal thermometry, respectively. In the experiments, water at room temperature was used as a test fluid and the test cylinders were heated with uniform heat fluxes. The local heat transfer coefficients were also measured with thermocouples to investigate the correlation between flow fields and local heat transfer characteristics over cylinders. The results show that three-dimensional flow separations occur first at the trailing edge of the cylinder when modified Rayleigh numbers of the cylinders exceed 2.1×10^9 , and that the separation points shift upstream with increasing Rayleigh numbers. The above separations become a trigger to the turbulent transition and transitional and fully turbulent flows appear downstream of the separation at higher Rayleigh numbers. Moreover, it was revealed that the local heat transfer coefficients in the transitional and turbulent regions are increased significantly compared with those in the laminar region.

Although these results will provide basic information on the mechanisms and also on the condition of the turbulent transition, several problems remain unsolved. One such problem is the effect of Prandtl number on the turbulent transition. In many practical situations, various fluids are utilized as working fluids for heating and cooling. However, we have little knowledge on the transition and the turbulent heat transfer of fluids with different Prandtl numbers. Among these fluids, air is most widely used. These motivate the present experiments with air. In order to investigate the turbulent transition and the local heat transfer characteristics of natural convective flows of air, we performed experiments in the wide range of Rayleigh numbers from 1.0×10^8 to 5.5×10^{11} . Cylinders having

Article by Misumi, Ref. 3.4-6

diameters from 200 mm to 1200 mm were fabricated and tested. The experiments begin with the visualization of flows using smoke to obtain basic information on turbulent transition mechanisms over cylinders. Then, local heat transfer coefficients were measured to investigate the correlation between flow fields and local heat transfer characteristics over cylinders. These results for air were next compared with the previous results for water and the effects of Prandtl number on the turbulent transition and also on the local heat transfer were discussed.

Nomenclature

D	diameter of cylinder
g	gravitational acceleration
h_m	overall heat transfer coefficient, $q_w/(T_{wm} - T_\infty)$
h_θ	local heat transfer coefficient, $q_w/(T_{w\theta} - T_\infty)$
Nu_m	average Nusselt number, $h_m D/\lambda_{fm}$
Nu_θ	local Nusselt number, $h_\theta D/\lambda_{f\theta}$
P	averaged axial pitch of separation
Pr	Prandtl number
q_w	wall heat flux
Ra_D	Rayleigh number, $g\beta(T_w - T_\infty)D^3/(\alpha\nu)_{fm}$
Ra_D^*	modified Rayleigh number, $g\beta q_w D^4/(\lambda\alpha\nu)_{fm}$
T	temperature
$T_{w\theta}$	local wall temperature at location θ

Greek symbols

α	thermal diffusivity of fluid
β	coefficient of volume expansion
θ	angle from cylinder bottom
λ	thermal conductivity of fluid
ν	kinematic viscosity of fluid

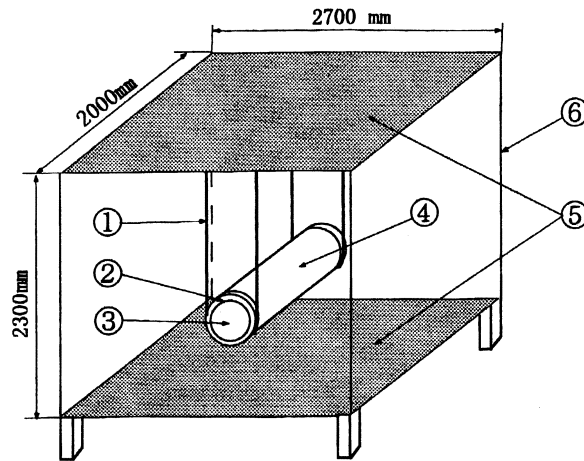
Subscripts

c	critical
fm	at average film temperature
$f\theta$	at local film temperature
m	average
w	wall
θ	at angular location θ
∞	at ambient

2. Experimental Apparatus and Measurements

The present experimental apparatus is schematically illustrated in Fig. 1. The apparatus consisted of a test cylinder and a test chamber. Preliminary experiments showed that natural disturbance in the environmental air exerts serious influences on the transition of flows around cylinders. Thus, in order to suppress the disturbance as small as possible, a specially designed test chamber was fabricated and used in the present experiments. The test chamber is 2.7 m long, 2 m

Article by Misumi, Ref. 3.4-6



1. Band 2. Resin Pipe 3. Insulation
 4. Test Cylinder 5. Punched Metal Plate
 6. Measurement Chamber

Fig. 1. Experimental apparatus.

wide, and 2.3 m high and the test cylinder was placed horizontally in the chamber. The walls of the chamber were made of plywood plates and an acrylic resin plate, while the floor and the ceiling were made of stainless-steel plates punched with holes 3 mm in diameter. The chamber was placed 400 mm above the laboratory floor.

The floor and ceiling of the test cylinder were fabricated with solid plates, a thermal plume arose from the heated cylinder and impinged on the ceiling, and air then circulated in the chamber. This caused a high level of turbulence as well as thermal stratification of air within the chamber. Meanwhile, the plume will be easily exhausted from the chamber by the use of a punched ceiling, and fresh air with small turbulence will be introduced into the chamber through the punched floor. The visual observation with smoke confirmed that the above through-flow does occur in the test chamber. In addition, we changed the test cylinder with belts. The use of belts was aimed to move flow obstacles away from the chamber and to keep the turbulence level of air as low as possible.

The test cylinder was fabricated with a hollow pipe of acrylic resin 4 mm thick and stainless-steel foil heaters 30 μm thick. The heaters were glued on the outer surface of the cylinders and were connected in series. A uniform heat flux condition was realized by supplying AC power to the heaters. Styrofoam thermal insulation was glued on the inner surface of the pipe to reduce the conduction heat loss. Cylinders of diameters 200, 300, 400, 500, 800, and 1200 mm were prepared to enable experiments in a wide range of modified Rayleigh numbers, while the length of the cylinder was held at 850 mm.

For the sake of flow visualization, a smoke generator was fabricated. The generator consisted of an electric heater and a flask that contains liquid paraffin. The liquid paraffin evaporates and generates fine mists by heating the flask. The mist then enters a cooling chamber, where it is cooled to room temperature, and flows into a slot via an air pump. The slot (2 mm wide and 300 mm long)

was placed at the leading edge of the cylinder. The mist issued from the slot reflects the light and high-contrast pictures can be taken. A flow control valve was used to adjust the flow rate of smoke so as not to disturb the flow field.

Meanwhile, for the purpose of the heat transfer measurements, local surface temperatures of the heated cylinders, $T_{w\theta}$, were measured with Chromel–Alumel thermocouples of 100- μm diameter. They were spot-welded on the back of the heaters along the periphery of the cylinder at angular intervals of 5 to 10°. Thermocouples of the same material and diameter as above measured the temperatures of the ambient fluid, T_∞ . They were placed 200 mm apart from the cylinder with a vertical interval of 500 mm. Preliminary experiments showed that the conduction heat loss from the inner surface of the cylinders was less than 5% of the total heat generation on the heaters. Thus, surface heat fluxes of the cylinder q_w were calculated from input electrical power to the heaters Q , and the total surface area of the cylinder A , as: $q_w = Q/A$, by neglecting the conduction heat loss. Meanwhile, the heat deposited on the surface is transferred through convection and radiation. The heat flux by radiation q_r can be estimated as

$$q_r = \sigma \epsilon (T_{w\theta}^4 - T_\infty^4) \quad (1)$$

where σ and ϵ denote the Stefan–Boltzmann constant and the emissivity of the stainless-steel heaters, respectively. In order to calculate q_r from the above equation, ϵ should be determined precisely. Thus, the temperature of the stainless-steel heater was measured with both a thermo-camera and a thermocouple simultaneously. Then, the output temperature of the thermo-camera was adjusted so as to coincide with the temperature from the thermocouple by varying the emissivity index of the thermo-camera. The value $\epsilon = 0.16$ was obtained from the above experiment. The value also coincides fairly well with that recommended in the handbook. Thus, we adopted the above value as the emissivity of the present cylinders. By subtracting the above radiation heat flux q_r from the total surface heat flux q_w , the convective heat flux q_c was calculated as: $q_c = q_w - q_r$. Then, the local heat transfer coefficient h_θ at angular location θ from the cylinder bottom was defined by using the above q_c as:

$$h_\theta = q_c / (T_{w\theta} - T_\infty) \quad (2)$$

In the present experiments, the temperatures of the cylinder surface $T_{w\theta}$ and the ambient air temperatures T_∞ have been monitored with a pen-recorder. The results showed that a steady state is realized about 4 and 15 hours after heating for the cylinders of 200- and 1200-mm diameter, respectively. We have carried out the visualization and heat transfer experiments in this steady state. To keep the ambient temperature constant, the experiments were conducted at midnight on a cloudy day. Moreover, in order to minimize the heat loss by conduction and radiation, and also to carry out measurements with high accuracy, the temperature difference between the cylinder surface and ambient fluid was kept within 25 K throughout the run. Regarding the measurements of heat transfer coefficients in the transition and turbulent regions, the surface temperatures were recorded for more than 300 seconds and they were averaged to yield the mean temperatures. Thermophysical properties in nondimensional parameters mentioned below were estimated at the film temperatures as: $T_f = (T_w + T_\infty)/2$, while the coefficient of volume expansion β was calculated at the ambient temperature as: $\beta = 1/T_\infty$.

3. Results and Discussion

3.1 Visualization of flow fields over cylinders

The flows over heated cylinders were visualized first with smoke to obtain basic information on the turbulent transition mechanisms over cylinders. Typical results are presented in Fig. 2. To visualize the flow field two-dimensionally, a slot was installed at the bottom or side of the cylinders. Figure 2(a) represents the flow field around a 300-mm cylinder. The smoke issued from the slot first flows along the cylinder surface, subsequently detaches from the trailing edge of the cylinder, and finally ascends as a laminar plume. The figure also shows that a laminar boundary layer covers the whole surface of the cylinder. When the diameter of the cylinder was increased to 500 mm, the smoke ascending along the cylinder surface separates three-dimensionally from the trailing edge of the cylinder, and forks into many filaments as shown in Fig. 2(b). Similar separations are also observed over the cylinders of 800 and 1200 mm diameter as shown in Figs. 2(c) and 2(d). The separation points shift sideward on the cylinder with an increase in diameter. Moreover, Fig. 2(d) demonstrates that the smoke filaments after separation fluctuate irregularly, and a fully turbulent state is realized at a certain distance from the separation. The flow still ascends along the surface and leaves from the trailing edge of the cylinder.

The above figures reveal that three-dimensional separation becomes a trigger to the turbulent transition and that the turbulent flows appear downstream of the separation. Similar transition phenomena as above have been reported in the previous experiments with water [3]. However, we observed that the separation points of air move more vigorously than water and they are affected seriously by the natural disturbance of the ambient air. Thus, for the sake of the precise measurements of the onset of separation and also of the pitches of separation, the natural disturbance should be kept as low as possible. Thus, we have exercised special caution to reduce the disturbance as mentioned in the previous section. These procedures enabled intensive investigation on the three-dimensional separation mentioned in the text.

One of the particular concerns of the present study is the three-dimensional separation at the trailing edge, because the condition will yield the onset of the turbulent transition. In order to determine this condition, visualization experiments were performed with the cylinders of 300 and 400 mm diameter by varying the heat flux systematically. The results showed that three-dimensional separation occurs when the modified Rayleigh numbers of the cylinders Ra_D^* exceed 3.5×10^9 . The value is somewhat higher than that of water $Ra_D^* = 2.2 \times 10^9$.

The separation points shift from the trailing edge to the sides of the cylinders with the Rayleigh numbers. The separation points are another concern of the present study, because the flows over the cylinder can be classified into the upstream laminar flow and the downstream transitional and turbulent flows according to the separation points. Thus, we next investigated the separation points under the various conditions of cylinder diameters and surface heat fluxes. The separation points, however, show marked variations in the spanwise direction, so that the pictures were taken first by video recorder for a long period, and then the angular locations of the separation were measured from the reproduced pictures with an interval of 5 s. The measurements were repeated 50 to 60 times and their average locations were defined as the separation points. The results are presented in Fig. 3, where

Article by Misumi, Ref. 3.4-6

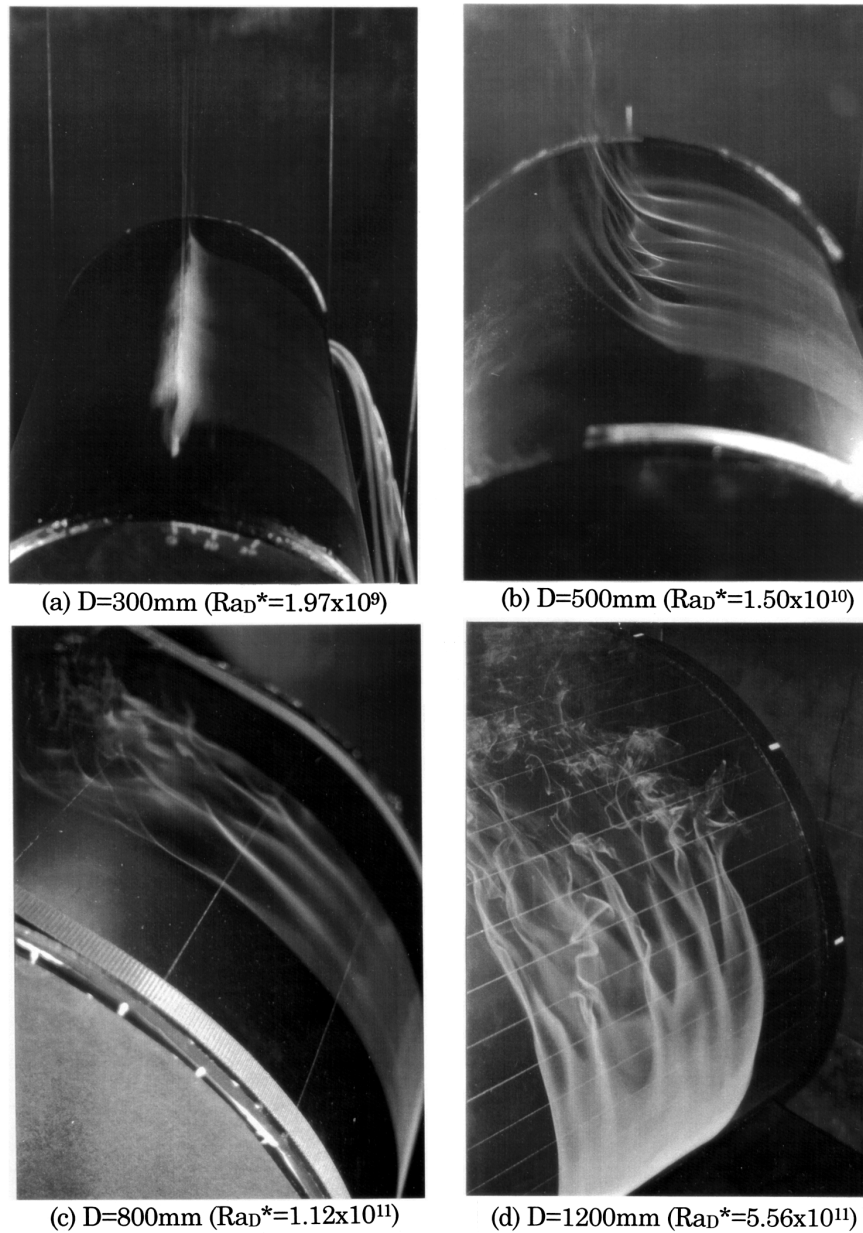


Fig. 2. Visualized flow fields around cylinders.

the angles of separation points θ measured from the leading edge of the cylinder are plotted in terms of the modified Rayleigh numbers Ra_D^* together with the previous results for water.

The figure shows that the separation points of air first appear at $\theta = 180^\circ$ when $Ra_D^* = 3.5 \times 10^9$, and they gradually shift sideward in the cylinder with increasing Rayleigh numbers. However, they remain at around $\theta = 95^\circ$ even at the maximum Rayleigh number of the present experiments

Article by Misumi, Ref. 3.4-6

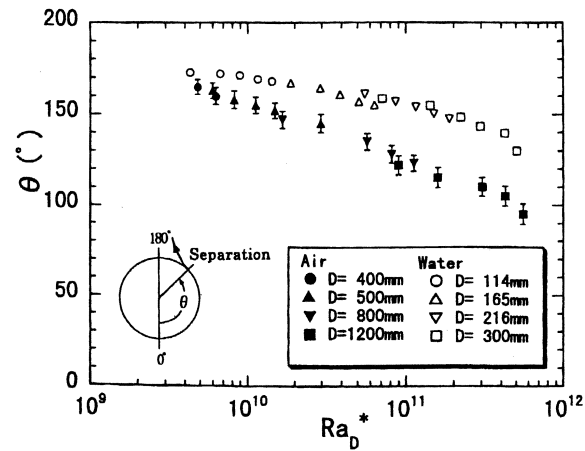


Fig. 3. Onset of three-dimensional separation.

$Ra_D^* = 5.5 \times 10^{11}$, indicating that the transitional and turbulent regions occupy one-half of the total surface area. Moreover, it is obvious from the figure that the separation of air occurs upstream of water.

The next concerns were axial pitches of three-dimensional separation. As was demonstrated in Fig. 2, the smoke filaments behind the separation appear at almost constant pitches. It is of physical importance to investigate the pitches of the filaments. Thus, we measured the pitches under various conditions of cylinder diameters and surface heat fluxes. With the same procedures mentioned previously, the values were averaged to yield the mean axial pitches. In the present experiments, the mean axial pitches P ranged from 60 to 100 mm, and they become larger with the diameter and smaller with the heat flux. The values are far larger than those of water, $P = 6$ to 21 mm. Referring to the previous results on water, the present pitches of air were normalized with the length scale, $le = (\alpha\nu\lambda/g\beta q_w)^{1/4}$. The results are plotted in terms of Ra_D^* and are shown in Fig. 4. The error bars in the figure show the standard deviations of data. As is apparent from the figure, normalized pitches become almost constant for both water and air, while absolute values of the pitches for air are twice those of water.

3.2 Local heat transfer coefficients of cylinders

In light of the above results on the flow visualizations, we subsequently measured the local heat transfer coefficients using thermocouples. The experiments were carried out with cylinders of 200 to 1200 mm diameter and under various surface heat fluxes. Typical results are presented in Fig. 5 for the case of constant heat flux $q_w = 100 \text{ W/m}^2$, and of variable cylinder diameters. The local Nusselt numbers divided by the 1/5th power of the modified Rayleigh numbers, $Nu_\theta/Ra_D^{*1/5}$, are plotted in terms of the angles from the bottom, θ .

The local Nusselt numbers for the 200- and 300-mm cylinders show the maximum to be at the leading edge and decrease monotonously with the angle. This is due to the development of a

Article by Misumi, Ref. 3.4-6

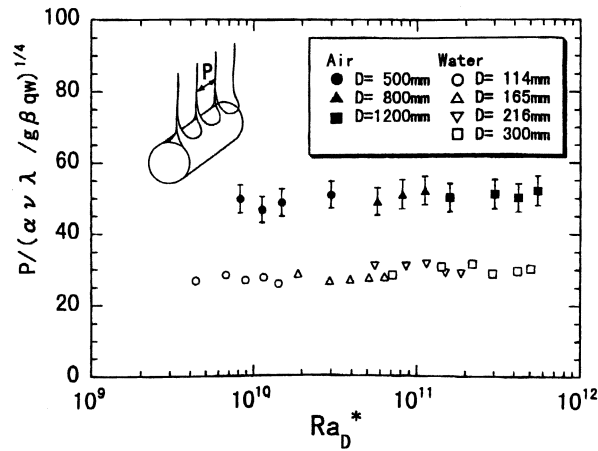


Fig. 4. Mean axial pitch of separation.

laminar boundary layer over the cylinders. Since the modified Rayleigh numbers of these cylinders are less than the critical Rayleigh number, $Ra_D^* = 3.5 \times 10^9$, the laminar boundary layer covers the whole surface. Similar variations in the local Nusselt numbers are also observed in the bottom and side regions of 400- and 500-mm cylinders. However, the Nusselt numbers of the 400- and 500-mm cylinders depart from the above laminar plots at angles θ beyond 160° and 150° , respectively. The regions of the increased Nusselt numbers gradually expand upstream with further increase in the cylinder diameter as is obvious from the data for the 800- and 1200-mm cylinders. Comparing these results with those of the flow visualization, we confirmed that the marked increase in the local Nusselt numbers begins with the three-dimensional separation.

We next discuss the local Nusselt numbers downstream of the separation. As shown in Fig. 5, the Nusselt numbers of 1200-mm cylinders begin to increase at $\theta = 120^\circ$, and reach a maximum at around $\theta = 150^\circ$. Then, they begin to decrease and show gradual increase toward the trailing edge. Similar variations in the Nusselt numbers were also observed in the previous experiments with water [4]. The previous measurements were performed on the higher Rayleigh numbers $Ra_D^* = 3.6 \times 10^{13}$, which is almost two decades higher than in the present experiments, $Ra_D^* = 5.5 \times 10^{11}$. The result showed that the Nusselt numbers in the fully turbulent region become constant. On the other hand, we cannot recognize that such a region exists over the 1200-mm cylinder. The result suggests that fully turbulent flow may not be realized even for the maximum Rayleigh number of the present experiments.

3.3 Average heat transfer coefficients

Based on the local Nusselt numbers obtained above, we calculated the average Nusselt numbers of the cylinders. The results are shown in Fig. 6 in terms of the modified Rayleigh numbers. As mentioned in Section 1, several researchers have proposed correlation equations for the average Nusselt numbers. These equations are applicable to both the laminar and turbulent heat transfer. For comparison, the equations proposed by McAdams [4], Morgan [5], and Churchill and Chu [6] are

Article by Misumi, Ref. 3.4-6

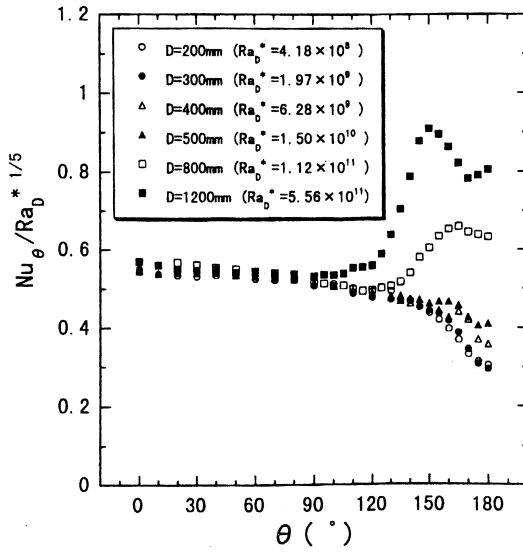


Fig. 5. Local Nusselt numbers of cylinders.

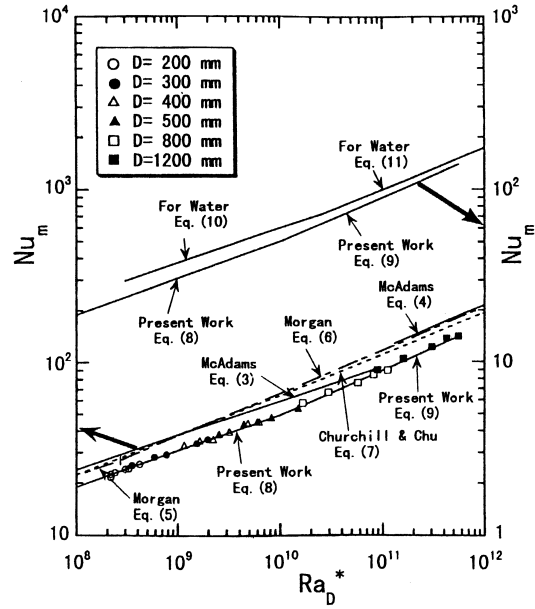


Fig. 6. Average Nusselt numbers of cylinders.

represented as lines in the figure. In order to compare the present results for the uniform heat flux cylinders with the previous results for the isothermal cylinders, the latter equations are transformed using the relation $Ra_D^* = Ra_D \cdot Nu_D$. The equations are then expressed as follows:

McAdams [4]:

$$Nu_m = 0.597 Ra_D^{*1/5} \quad (\text{where } 5.3 \times 10^4 < Ra_D^* < 9.3 \times 10^{10}) \quad (3)$$

$$Nu_m = 0.215 Ra_D^{*1/4} \quad (\text{where } 1.3 \times 10^{11} < Ra_D^* < 1.3 \times 10^{15}) \quad (4)$$

Morgan [5]:

$$Nu_m = 0.556 Ra_D^{*1/5} \quad (\text{where } 4.8 \times 10^4 < Ra_D^* < 2.7 \times 10^8) \quad (5)$$

$$Nu_m = 0.210 Ra_D^{*1/4} \quad (\text{where } 2.7 \times 10^8 < Ra_D^* < 1.3 \times 10^{15}) \quad (6)$$

Churchill and Chu [6]:

$$Nu_m^{1/2} = 0.60 + 0.321 (Ra_D^* / Nu_m)^{1/6} \quad (7)$$

In the derivation of Eq. (7), $Pr = 0.7$ was assumed in their original equation for simplicity and the value corresponds to the present experimental Pr number. Equation (7) is applicable to both laminar and turbulent flows.

Article by Misumi, Ref. 3.4-6

As is obvious from Fig. 6, the present results show 15 to 20% smaller Nusselt numbers than those estimated from the previous empirical equations, and they can be correlated with the following two forms:

$$Nu_m = 0.40Ra_D^{*0.21} \quad (\text{where } 1.0 \times 10^8 < Ra_D^* < 1.0 \times 10^{10}) \quad (8)$$

$$Nu_m = 0.126Ra_D^{*0.26} \quad (\text{where } 1.0 \times 10^{10} < Ra_D^* < 5.5 \times 10^{11}) \quad (9)$$

The previous workers have defined the critical Rayleigh numbers for the turbulent transition with the Rayleigh numbers corresponding to the deflection points of the average Nusselt numbers plotted on the $\log Nu_m - \log Ra_D^*$ plane. Based on this definition, the present critical Rayleigh number becomes $Ra_D^* = 1.0 \times 10^{10}$. However, the present visualization revealed that the actual transition begins at a smaller Rayleigh number, $Ra_D^* = 3.5 \times 10^9$. The above discrepancy in the critical Rayleigh numbers can be explained as follows. The local Nusselt numbers are increased, in fact, in the transitional and turbulent regions; however, these regions occupy only a small portion of the cylinder surface, and, thus, the average Nusselt numbers remain unchanged from the laminar values. Taking account of this, the critical Rayleigh numbers based on the average Nusselt numbers seem inaccurate.

We next discuss the discrepancy in the average Nusselt numbers between the present results and the previous empirical equations. Although exact reasons for this discrepancy are uncertain, one of the possible reasons is due to the inappropriate derivation of the previous correlation equations. For instance, McAdams proposed Eqs. (3) and (4) together with the data plotted on the $Nu_m - Ra_D$ plane. However, we cannot find any descriptions on the test cylinders, working fluid, and measurements in his textbook [4]. Morgan derived Eqs. (5) and (6) by simply averaging the existing heat transfer data obtained by others. However, the data show considerable scatter between the researchers, so that a simple average of the data may cause deviation from the real Nusselt numbers. The circumstances are the same for Eq. (7) proposed by Churchill and Chu. They obtained the equation so as to coincide with the experimental results of Kutateladze [7], who conducted heat transfer experiments in the high-Rayleigh-number region. However, referring to the original textbook of Kutateladze, there was no description on the experimental apparatus and measurement techniques. Thus, it is doubtful whether the previous empirical equations can predict the Nusselt numbers correctly.

We next discuss the Prandtl number effect on the overall heat transfer. In this regard, the average Nusselt numbers for water [3] are compared with the present Nusselt numbers. The results are plotted as the lines in Fig. 6. Here, the average Nusselt numbers for water can be expressed as follows:

$$Nu_m = 0.60Ra_D^{*0.2} \quad (\text{where } 3.0 \times 10^8 < Ra_D^* < 2.5 \times 10^{10}) \quad (10)$$

$$Nu_m = 0.23Ra_D^{*0.24} \quad (\text{where } 2.5 \times 10^{10} < Ra_D^* < 3.6 \times 10^{13}) \quad (11)$$

As is obvious from the figure, the Nusselt numbers for water are higher than for air. This result is mainly due to the laminar heat transfer around cylinders. Kuehn and Goldstein [8] investigated the Prandtl number effect on the laminar heat transfer by numerical analysis. Their results showed that

Article by Misumi, Ref. 3.4-6

the Nusselt numbers of the laminar flows increase with the Prandtl number of the fluid. Taking account of the fact that the laminar flow covers a considerable portion of the present cylinder, the average Nusselt numbers for water, $Pr = 6$, will become higher than for air, $Pr = 0.7$.

The difference in the average Nusselt numbers between water and air gradually becomes gradually smaller with increasing Rayleigh numbers. This is attributed to the extension of the transitional and turbulent regions. Figure 3 revealed that the turbulent transition of air occurs far upstream of water, in particular, in the high-Rayleigh-number region. Thus, the transition and turbulent regions cover broader surface area for air, where heat transfer is enhanced significantly. This explains the above increase in the Nusselt numbers of air with the Rayleigh numbers.

It should be noted that the heat transfer is affected seriously by the Prandtl number of the fluid even in the region of high Rayleigh numbers. In view of this, the previous empirical equations seem incomplete, because the Prandtl number effects have not been accounted for in those equations. Meanwhile, Eqs. (8) to (11) have been proposed from the comprehensive heat transfer results taken from cylinders of various diameters and also from fluids of different Prandtl numbers. Therefore, the results provide reliable data on the overall heat transfer for both water and air.

4. Conclusions

The fluid flow and the heat transfer of natural convection around large horizontal cylinders were investigated experimentally in the current study. Special concerns were the high-Rayleigh-number flows that undergo turbulent transition. In order to investigate the conditions of turbulent transition and also the transition mechanisms, the flow fields over the cylinders were visualized with smoke. Measurements of the local heat transfer coefficients were subsequently carried out to investigate the relation between the visualized flow fields and the local heat transfer characteristics. Test fluid was air at room temperature. The cylinders were heated with uniform heat fluxes. The diameter of the cylinders was varied from 200 to 1200 mm so as to conduct experiments over a wide range of modified Rayleigh numbers from 1.0×10^8 to 5.5×10^{11} . The results are summarized as follows.

(1) The flow visualizations with smoke revealed that the following phenomena appear over the cylinders when the Rayleigh numbers are high enough. (i) Laminar boundary layer develops over the cylinder from the leading edge to the separation point. (ii) The boundary layer then separates three-dimensionally from the surface. (iii) Transitional flow appears downstream of the separation. (iv) The flow after separation fluctuates irregularly and a fully developed turbulent flow is realized near the top of the cylinder. (v) The turbulent flows ascending along both sides of the cylinder merge with each other near the trailing edge and ascend away from the cylinder as a turbulent plume. These transition phenomena are similar to those reported in the previous experiments with water.

(2) The above results suggest that the three-dimensional separation becomes a trigger to the turbulent transition of natural convection for both air and water. The present separation first appears at the trailing edge of the cylinders when $Ra_D^* = 3.5 \times 10^9$. When the Rayleigh number is less than the above, the flow remains laminar throughout the circumference of the cylinder. When the Rayleigh number exceeds the above critical number, three-dimensional separation takes place and the separation points shift upstream of the cylinder with further increase in the modified Rayleigh numbers.

Article by Misumi, Ref. 3.4-6

(3) The local heat transfer coefficients from the cylinders were also measured with thermocouples. It was revealed that the local Nusselt numbers in the laminar regions increase in proportion to $Ra_D^{*1/5}$. The numbers increased markedly from the laminar values in the transitional and turbulent regions.

(4) Based on the above local Nusselt numbers, correlation equations for the average Nusselt numbers were proposed. The present results show 15 to 20% smaller Nusselt numbers than those estimated from the previous empirical equations in the ranges of the Rayleigh numbers, $1.0 \times 10^8 < Ra_D^* < 5.5 \times 10^{11}$.

Literature Cited

1. Farouk B, Guceri SI. Natural convection from a horizontal cylinder-turbulent regime. *Trans ASME J Heat Transfer* 1982;104:228–235.
2. Hattori Y. Turbulent natural convection boundary layer around horizontal cylinder. *Proc National Heat Transfer Conf Japan* 1996;33:853–854. (in Japanese)
3. Kitamura K, Kami-iwa F, Misumi T. Heat transfer and fluid flow of natural convection around large horizontal cylinders. *Int J Heat Mass Transfer* 1999;42:4093–4106.
4. McAdams WH. *Heat transmission*, 3rd ed. McGraw–Hill; 1954. p 175–177.
5. Morgan VT. *Advances in Heat Transfer* 1975;11:199–210. Academic Press.
6. Churchill SW, Chu HS. Correlation equations for laminar and turbulent free convection from a horizontal cylinder. *Int J Heat Mass Transfer* 1974;18:1049–1053.
7. Kutateladze SS. *Fundamentals of heat transfer*. Academic Press; 1963. p 293.
8. Kuehn TH, Goldstein RJ. Numerical solution to the Navier–Stokes equations for laminar natural convection about a horizontal isothermal circular cylinder. *Int J Heat Mass Transfer* 1980;23:971–979.



Originally published in *Trans JSME Ser B* **65**, 1999, 1010–1017.

Translated by Toshiyuki Misumi, Department of Mechanical Engineering, Kagoshima National College of Technology, 1460-1 Shinko, Hayato-cho, Kagoshima, 899-5102 Japan.

RAI 3-6

Perform the thermal evaluation for Normal Conditions of Transportation (NCT) for all DSCs proposed for payload in the NUHOMS-MP197 transportation package using the maximum heat load for transport for each DSC type.

The SAR only includes thermal evaluation during NCT for both 37PTH and 69BTH. Page A.3-67 of the SAR states: "The DSC types 61BTH, 61BT, 32PTH, 32PTH1, 32PT, 24PTH, and 24PT4 are evaluated previously for normal transfer conditions under 10 CFR Part 72 requirements. The DSC shell temperature profiles of these DSCs in MP197HB model are compared with the corresponding profiles from 10 CFR Part 72 SARs in Section A.3.6.3 of the SAR. It is shown that the fuel cladding and the basket component temperatures in 10 CFR Part 72 SARs represent the bounding values for these DSCs under transport conditions. Therefore, no additional analysis is performed for the DSCs previously evaluated under 10 CFR Part 72 conditions. The maximum fuel cladding and the basket component temperatures for these DSCs are taken from 10 CR Part 72 SARs and reported as the bounding values for transport conditions." Section A.3.6.3 of the SAR provides a summary of the justification for using bounding temperature profiles. The SAR approach may increase uncertainty of predictions since the geometries of MP197HB transport cask and the storage transfer cask are different which may result in different DSC temperature profiles. The staff needs to have assurance the transport configuration for each DSC has been adequately analyzed in the SAR in order to make a determination on the predicted results.

This information is needed to determine compliance with 10 CFR 71.71.

Draft Response to RAI 3-6

The following discussion will be incorporated into the SAR.

Among the DSC types previously evaluated for storage applications and proposed for transport in the MP197HB, DSC type 24PTH-S (without aluminum inserts) has the smallest margin (19°F) for the maximum fuel cladding temperature under storage conditions and has the second highest heat load for transportation conditions (26 kW) after the 69BTH DSC (see SAR Table A.3-10). A thermal analysis of this DSC type under NCT is prepared to provide additional assurance that the justifications and evaluations reported in SAR Sections A.3.3.2 and A.3.6.3 are valid and the fuel cladding and the basket component temperatures in 10 CFR Part 72 SARs represent the bounding values for transport conditions.

Consistent with the approach described in SAR Section A.3.3.1.4, the DSC shell temperature profile for the 24PTH DSC is retrieved from the MP197HB cask model and applied as boundary conditions to the detailed model of the 24PTH-S DSC/basket. The DSC/basket model of 24PTH-S is identical to the model previously used for storage conditions in the 10 CFR Part 72 UFSAR [Ref. 3.6-1], Appendix P. A uniform heat load zone configuration with the maximum heat load of 26 kW is applied in the 24PTH-S DSC model. The results of this case are compared with the results used in the SAR to demonstrate the conservative nature of the approach.

Comparisons of the maximum DSC component temperatures are listed in the following table.

Comparison of the Maximum Temperatures for 24PTH-S DSC

DSC Type	24PTH-S (w/o Al inserts)		Additional Thermal Margin
	Uniform (1.3 kW/FA)	Uniform (1.08 kW/FA)	
Operating Condition	Normal Transfer 31.2 kW UFSAR [Ref. 3.6-1], Tables P.4-10, -14 and -16	NCT 26 kW	
	$T_{Transfer}$ (°F)	T_{NCT} (°F)	$(T_{Transfer} - T_{NCT})$ (°F)
Fuel Cladding	733	664	+69
Fuel Compartment	682	616	+66
Al/Poison	681	615	+66
DSC Shell	475	463	+12

As seen in the above table, the maximum fuel cladding and basket component temperatures for the DSC type 24PTH-S (without aluminum inserts) under NCT are more than 60°F lower than the bounding values listed in the UFSAR [Ref. 3.6-1]. This large difference demonstrates that the comparison of the DSC shell temperatures as discussed above is a conservative approach to bound the maximum fuel cladding and basket component temperatures for transport conditions.

References to Draft Response to RAI 3-6

- 3.6-1 Updated Final Safety Analysis Report for the Standardized NUHOMS® Horizontal Modular Storage System for Irradiated Nuclear Fuel, NUH-003, Rev. 11.

RAI 3-7

Perform a sensitivity study of all assumed gaps and explain how the assumed values for these gaps are maintained (within tolerances) at or below the values used for the thermal evaluation of the NUHOMS-MP197 transportation package. Specify how these gaps are maintained within expected tolerances.

The applicant's developed thermal models described in the SAR are based on a number of explicit gaps which, according to the applicant, bound the fabrication uncertainties and are kept within tolerances but an explanation on how these gaps are controlled is not provided in the SAR. A sensitivity study performed by the staff using confirmatory analysis models shows the peak cladding temperature is very sensitive to the gap sizes assumed in the analysis.

This information is needed to determine compliance with 10 CFR Part 71 (71.71 and 71.73)

Draft Response to RAI 3-7

The following discussion will be incorporated into the SAR.

Axial and radial gaps are considered in the MP197HB and DSC models. The axial gaps are located toward the ends of the cask and the radial gaps are located between the multiple shells of the cask, between the basket and the DSC shell, and between the sheets and tubes within the basket. The peak cladding temperature is more sensitive to the radial gaps since the cask ends are covered with impact limiters, which act as insulators.

A thermal test is planned to assure that the thermal performance of the as-built cask satisfies or exceeds the performance considered in the cask model in the radial direction. The lead pouring process requires that the lead is cooled from the bottom up, and a molten pool of lead remains at the top to fill gaps that form as the lead at the bottom solidifies. SAR Chapter A.8 will be revised to address the planned thermal test.

No changes were made to the gaps assumed in the DSC models approved previously under 10 CFR 72 regulations. The validities of these assumptions were reviewed by NRC in 10 CFR 72 applications.

The radial gaps considered in the 69BTH DSC model are described in SAR Section A.3.3.1.4 and are listed below.

Radial gaps in 69BTH DSC model:

- 69BTH-a) 0.30" diametrical hot gap between the basket outer surface and the canister inner surface.
- 69BTH-b) 0.01" gap between any two adjacent components (tubes, neutron absorbers, wraps, rails) in the cross section of the basket.
- 69BTH-c) 0.01" gap between the sections of the paired aluminum and poison plates in axial direction.
- 69BTH-d) 0.1" gap between the two small aluminum rails at the basket corners.

69BTH-e) 0.1" gap between the two pieces of large aluminum rails at 0° -180° and 90° -270° orientations.

The diametrical gap between the basket and canister shell assigned as gap 69BTH-a here is controlled by dimensional inspections of the diameters of the basket and canister shell. The size of gap 69BTH-a is justified in SAR Section A.3.6.7.3 and will be discussed further in response to RAI 3-11.

The gaps between adjacent basket components assigned here as gap 69BTH-b are shown in SAR Figure A.3-16 and in the figure on SAR Page A.3-136. The thermal model considers a uniform gap of 0.01" between any two adjacent components in the cross section of the basket. The structure of the 69BTH basket is similar to the 61BT and 61BTH baskets approved in accordance with 10 CFR 72 regulations. The same gap sizes were considered between adjacent components in the 61BT and 61BTH designs.

In practical terms, fabrication of the 69BTH basket requires very tightly compressed assembly in order to fit the basket into the shell. Interfaces are formed as components and parts are assembled. The fit between mating components, for example between fuel compartment tubes and adjacent sheets, cannot practically be measured. Fabrication methods provide for the tightest practical assembly of these parts.

The gaps between adjacent components are related only to the flatness and roughness tolerances of the plates. The micro gaps related to these tolerances are non-uniform and provide interference contact at some areas and gaps on the other areas as shown schematically in the figure on SAR Page A.3-131. For the purpose of thermal evaluation, surfaces of intermittent contact between adjacent components are conservatively modeled as a uniform gap of 0.01". As shown in SAR Section A.3.6.7.4, the assumed gap size of 0.01" is approximately two times larger than the contact resistances between the adjacent components. It should be noted that for conservatism no contact pressure was considered between the components. This assumption implies that no friction exists between the components within the basket, which adds to the conservatism considered in the size of this uniform gap. In reality, there is sufficient friction that 61BT baskets have been lifted during fabrication using only the friction on the perimeter of the four-compartment subassemblies.

The 0.01" axial gaps between the sections of the paired aluminum and poison sheets assigned here as gap 69BTH-c are shown in SAR Figure A.3-17. The 0.1" gaps between the rail segments assigned here as gaps 69BTH-d and 69BTH-e are shown in SAR Figure A.3-15. These gaps are not located in the primary heat flow paths. A sensitivity analysis is performed to determine the effect of these gaps on the thermal performance. The results of this sensitivity analysis summarized in the following table shows that doubling the size of these gaps increases the maximum temperatures by less than 1 °F. Therefore, the effect of these gaps on the thermal performance is insignificant.

Results of the Sensitivity Analysis

	T _{max, Fuel} (°F)	T _{max, Comp} (°F)	T _{max, Al/Poison} (°F)	T _{max, Rail} (°F)
69BTH, 32kW from SAR Table A.3-10	674.3	638.3	621.8	534.3
69BTH, 32kW gaps sizes 69BTH-c, -d, and -e doubled	674.5	638.5	622.0	534.3
Difference	+0.2	+0.2	+0.2	+0.0

The radial gaps considered in the 37PTH DSC model are described in SAR Section A.3.3.1.6 and are listed below.

Radial gaps in 37PTH DSC model:

- 37PTH-a) 0.45" diametrical hot gap between the basket outer surface and the canister inner surface.
- 37PTH-b) 0.01" gap between the basket rails and the compartment plates.
- 37PTH-c) 0.0075" gap between the poison/aluminum chevrons and the fuel compartments.

The size of gap 37PTH-a is larger than the nominal cold gap and is therefore conservative.

The gap between the basket rails and the compartment plates, assigned here as gap 37PTH-b, is shown in SAR Figure A.3-25. The basket rails are bolted to the basket plates. Therefore, very good contact is expected between the basket rails and basket plates. The contact resistance across this gap is related only to the flatness and roughness tolerances of the plates. As described above, the assumed uniform gap size of 0.01" is approximately two times larger than the contact resistances between these components.

The structure of the 37PTH basket is similar to the 32PT basket approved in accordance with 10 CFR 72 regulations. Identical to the 32PT basket, the "L" shaped poison/aluminum plates are bolted to the compartment plates in the 37PTH basket. Therefore, good contact is expected between the chevrons and the compartment plates. The gap size of 0.0075", assigned here as gap 37PTH-c, is the same size that was considered between the "L" shaped poison/aluminum plates and the compartment plates in the 32PT basket design.

RAI 5-8:

Demonstrate via calculation that the source terms calculated using the SAS2H code are conservative given the fact that there are about 11% uncertainties in the SAS2H calculation.

On page A.5-6 of the revised SAR, the applicant states: AReference [13] documents that SAS2H tends slightly to over predict the concentration of ^{244}Cm when burnup is varied during the sensitivity study. Therefore, as the ^{244}Cm isotope accounts for more than 90% of the total neutron source term, the uncertainty in the neutron source and associated neutron dose rates is expected to be less than $\forall 11\%$.@ On the same page, the applicant further states: AThe uncertainty value of 10% is an uncertainty in the ability of the SAS2H code to predict the isotopic concentration of nuclides in the fuel. In many cases, this results in SAS2H over-predicting the quantity of certain fission product or actinide isotope, thereby resulting in a conservative prediction of source terms. These benchmarks demonstrate that the neutron spectrum calculated by SAS2H during depletion is appropriate for the purpose of source term calculations. An uncertainty has not been applied in the dose rate calculations.@ The staff reviewed this assertion and compared it with the results from the relevant publications [Ref. 1, 2, 3] and found the conclusion inaccurate. For some of the isotopes, i.e., the major gamma emitters such as ^{154}Eu , and ^{155}Eu , SAS2H on average actually underestimates the concentrations by about 7.8% and 42.6%. For the dominant neutron emitter ^{244}Cm , SAS2H actually underestimates the concentration by 19.4%. Therefore, the assertion that SAS2H always over-predicts isotopic concentration is not acceptable. The applicant is requested to demonstrate that SAS2H always over-predicts isotopic concentrations for major fission products and actinides. Otherwise adjustments to the source terms must be made and the cask dose rates must be recalculated based on the new source term data.

This information is needed for the staff to determine if the package design meets the regulatory requirements of 10 CFR 71.47 and 71.51.

Draft RAI 5-8 Response:

The purpose of the discussion in Section A.5-2 (Page A.5-6 and A.5-8) on the uncertainty associated with the SAS2H predicted source terms is to provide a basis for the qualification of the computer code / cross section library for source term calculation. Neutron and gamma source terms are obtained as a result of irradiation of the fuel assembly and associated hardware materials. The most important parameters from a source term calculation standpoint are the material specifications and total irradiation. In addition, the production / decay chain for some of the important nuclides be accurate enough to ensure that the source terms are calculated accurately.

For spent fuel assemblies with cooling time greater than 6 years, the most important isotopes that contribute to most of the gamma radiation are ^{90}Sr , ^{90}Y , ^{106}Rh (^{106}Ru), ^{137}Cs , ^{144}Pr (^{144}Ce), ^{154}Eu , and ^{155}Eu . In addition, almost all of the light element source terms in the active fuel region and the total source terms in the fuel hardware regions are due to ^{60}Co . The dominant isotope from a

neutron source standpoint is ^{244}Cm . Numerous studies have been performed to determine the ability of the SAS2H/ORIGEN-S modules employing the 44 group ENDF/B-V cross section library in the accurate prediction of isotopic number densities. The calculation of isotopic number densities is important from a criticality standpoint for burnup credit evaluations and is dependent not only on the total irradiation but also on the fuel assembly design and neutron spectrum during irradiation.

The results of the isotopic assay evaluations are summarized in various NUREG /ORNL documents including the ORNL/TM-13315 document referenced by the staff. These evaluations conclude that the isotopic assay predicted by SAS2H is accurate to within 10% of the measured values. In some cases the concentrations of some of major gamma emitters are underpredicted, however, they are compensated by the overprediction of some of the other major gamma emitters. Therefore the assertion that SAS2H always overpredicts the concentration of major gamma emitters is not accurate and will be removed from the SAR. However, SAS2H prediction of the major gamma emitters is such that the resulting total gamma source term (and the effect on gamma dose rates) is conservative. For neutrons, the comparison to other isotopic assay benchmarks with ^{244}Cm indicates that SAS2H predictions are generally acceptable (the 19.4 % underprediction documented in ORNL/TM-13315 is closer to the measurement uncertainty of 15.5%).

A comparison of the various isotopic assay benchmarks indicates that SAS2H accurately predicts the concentration of major gamma and neutron emitters from a source term standpoint. In addition, a more direct validation of source term calculations is to measure the dose rate from these sources. Numerous measurements from various spent fuel storage and transportation systems have indicated that the measured dose rates are typically lower than calculated dose rates.

In summary, the source terms calculated by the SAS2H/ORIGEN-S modules is conservative because of the use of bounding material specification parameters employed in the models (maximize Co-60, maximize initial Uranium content). The comparison to isotopic assay data indicates that the SAS2H methodology is capable of accurately predicting the isotopic composition of nuclides important from a source term standpoint. Therefore, no other adjustments are made to the source terms calculated from SAS2H.

The SAR section A.5.2 is modified to include this discussion on the gamma and neutron source terms.

RAI 5-18:

Pertinent to the response function method, provide:

1. Detailed information on the definition of the response function, including the mathematical formulation and analytical derivation of the equations.
2. Technical bases of this method, i.e., how and why this approach works.
3. Validation and verification of the method.
4. Or publications and references to demonstrate the validity of the methodology.

Through the Shielding Evaluation chapter, the applicant mentions in numerous places that Aresponse function@ is used in shielding calculation and fuel qualification. However, there is no definition provided for this method which seems to play a vital role in the shielding evaluation of this package design. It is not clear what the technical bases are for this approach and there is no reference provided for the validity of this method.

This information is needed for the staff to determine if the package design meets the regulatory requirements of 10 CFR 71.47.

Draft RAI 5-18 Response:

Section A.5.5.1 of the SAR provides a description of the response function methodology employed to determine the Fuel Qualification Tables (FQTs). As described in the SAR, the response function methodology is employed to determine the contribution of a spent fuel source term to the dose rate at 2 meters from the impact limiters of the MP197HB transportation cask. Cooling times of the spent fuel assemblies (acceptable burnup and enrichment combinations) are adjusted such that the resulting dose rates at 2 meters under NCT are approximately the same for all the DSCs.

A new Appendix is added to Chapter A.5 to provide the details of the response function methodology including the required validation.

An additional evaluation that includes the effect of modeling spent fuel with some actinide isotopes is discussed herein.

The spent fuel is modeled as fresh in the shielding evaluation when calculating number densities. The NRC has requested a sensitivity study of the effect of including burned fuel for calculating number densities in the shielding models. Because the effect of actinides on the dose rate is expected to be negligible, a simplified model is developed in which the effect of using fresh fuel for number densities versus burned fuel can be quantified.

The fuel is modeled as a sphere with a radius of 5 cm and no cladding. Fresh fuel is modeled as

UO₂ with a density of 10.96 g/cm³ and an enrichment of 3.8%. For the burned fuel model, all non-negligible actinides, such as U-235, U-236, U-238, Np-237, Pu-238, Pu-239, Pu-240, Pu-241, Pu-242 and Am-241 are included. A density of 10.96 g/cm³ is maintained for the burned fuel. The actinide concentrations were extracted from the SAS2H output used to generate the source. The neutron models are run with the NONU card to turn off subcritical neutron multiplication, which would be slightly different for burned fuel (the current SAR models also use the NONU card.)

The MP197HB is modeled as a spherical shield around the source. The spherical tally surface is 1 meter from the surface of the shield. The large spherical tally ensures relatively quick convergence. Results are provided in the table below. The ratio of the dose rate between the burned and fresh fuel model is 1.0 for all calculated dose rates. Therefore, it is concluded that it is acceptable to model burned fuel as fresh in shielding calculations.

	Burned		Fresh		Ratio
	Dose Rate (mrem/hr)	Relative error	Dose Rate (mrem/hr)	Relative error	
Neutron	1.28151E-09	1.2%	1.27907E-09	1.2%	1.0
(n,γ)	2.36997E-10	0.4%	2.35663E-10	0.4%	1.0
Gamma	5.98836E-16	2.1%	6.00411E-16	2.1%	1.0

RAI 6-5:

Revise the criticality evaluation in Section A.6 of the application to consider bounding damaged fuel configurations for canisters which are intended to transport damaged fuel.

Although the structural evaluation in Section A.2 demonstrates that intact fuel subject to the hypothetical accident conditions of 10 CFR 71.73 will not result in significant fuel reconfiguration (pending approval of the staff materials and structural reviewers), it is not clear that this evaluation applies for already damaged fuel. Additionally, it is not clear that the single- and double-ended rod shear configurations used in the damaged fuel evaluations for most canister designs adequately bound the possible reconfiguration of damaged fuel subject to '71.73 conditions. Since it is unclear what condition damaged fuel assemblies will be in prior to transport, the criticality evaluation should consider bounding reconfigurations that may increase reactivity. Bounding conditions may include, but are not limited to, rod pitch expansion, cladding loss, or removal of rods from the fuel lattice.

This information is required in order for the staff to ensure that the package will meet the criticality safety requirements of 10 CFR 71.55 and 71.59.

Draft Response to RAI 6-5:

Currently, damaged fuel assemblies are authorized in the 61BT / 61BTH / 69BTH / 24PT4 / 32PTH / 32PTH1/ 24PTH and 37PTH DSCs. The 32PT is not authorized for storage and transportation of damaged fuel assemblies.

The criticality analyses documented for the 61BT / 61BTH / 69BTH and 24PT4 DSCs employ the fresh fuel assumption. Further the damaged fuel criticality evaluation for these DSCs consider the effect of fuel rod failure including single and double ended rod shear, fuel pitch variation including addition and removal of rods (missing rods) and migration of fuel rods beyond the poison. In addition, calculations are also performed for fuel rod decladding configurations. Therefore, the damaged fuel evaluations documented for these DSCs in Appendix A.6.5.1, Appendix A.6.5.2 and Appendix A.6.5.3 are adequately bounding.

The criticality analyses for damaged fuel assemblies for the 32PTH / 32PTH1/ 24PTH and 37PTH DSCs is revised to include the effect of modeling damaged fuel assemblies under NCT and HAC. A detailed discussion on the fuel assembly modeling and results for intact fuel assemblies under HAC is provided in the Response to RAI 6-1. The difference between intact fuel assemblies under HAC (with fuel rod permanent plastic deformation and no clad failure) and damaged fuel under HAC (with possible clad failure) is evaluated from a criticality standpoint to determine additional loading curves for damaged fuel assemblies.

Additional modeling considerations for damaged assemblies include:

- single shear configuration

- double shear configuration
- fuel assemblies with missing rods
- de-cladding of fuel rods

Note that the optimum pitch has already been considered in the intact HAC models. Preliminary criticality analysis of the various additional damaged assembly configurations indicates that the missing rod and de-cladding considerations will result in an increase in k_{eff} of the system with damaged assemblies. The preliminary results have indicated that the loading curves for the damaged fuel assemblies are determined by adjusting the intact fuel HAC loading curves up by 5 to 10 GWD/MTU to cover for the change in k_{eff} .